**Key Points:**

- We image and quantify the palaeosurface and subsurface 3D geometry of pit craters in Australia that formed in the Late Jurassic
- Pit craters are physically connected to upper tips of igneous dikes or steeply dipping, dilatational portions of normal faults
- We find no apparent relationship between pit crater geometry and formation mechanism

# Seismic Reflection Data Reveal the 3D Subsurface Structure of Pit Craters

Craig Magee[1] , Corbin Kling[2] , Paul Byrne[3] , and Christopher A-L Jackson[4]

[1]School of Earth Science and Environment, University of Leeds, Leeds, UK, [2]Center for Earth and Planetary Studies, Smithsonian Institution, Washington, DC, USA, [3]Department of Earth and Planetary Sciences, Washington University in St. Louis, St. Louis, MO, USA, [4]Department of Earth and Environmental Sciences, University of Manchester, Manchester, UK

**Abstract** Pit craters are quasi-circular depressions observed on rocky and icy planetary bodies, as well as numerous asteroids. Pit craters are thought to form by overburden collapse into a subsurface cavity or volumetrically depleted zone. Importantly, the surface size and distribution of pit craters may provide an important record of otherwise inaccessible subsurface processes. However, because we cannot access the subsurface of many planetary bodies, we rely on physical and numerical models to infer processes linked to pit crater formation. Here, we use 3D seismic reflection data to quantify the palaeosurface and subsurface geometry of 59 Late Jurassic pit craters buried to depths of ~3 km within a sedimentary basin, offshore NW Australia. The pit craters are typically funnel-like, with an inverted conical upper section underlain by a pipe. Pit crater depths, that is, the height of inverted cone sections, correlate with their plan-view length, consistent with observations of pit craters elsewhere; this trend is rendered less apparent by later sediment-infilling. For the first time, we show some pit crater pipes connect to underlying igneous dikes or steeply dipping, likely dilatational portions of normal faults. Although some pit craters seemed to have formed due to faulting and others to dyking, they cannot be differentiated based on their surface expression. Our data also suggest pit crater size may not relate to the mechanical properties of the host material. Overall, we conclude that the surface expression of pit craters on Earth and other planetary bodies may not be diagnostic of subsurface processes or properties.

**Plain Language Summary** Linear chains of small craters are commonly observed on planetary bodies like Mars, Enceladus, or various asteroids. These depressions, called pit craters, are not related to meteorite impacts. Because pit craters are of a similar shape and size to features observed on Earth and created in laboratory models, we think they form when rock collapses into holes present beneath the surface. Previous studies have not been able to work out how these holes form, because we cannot easily look beneath the surface of other planetary bodies. In this study we use a technique called seismic reflection, which uses sound waves to create an ultrasound-like 3D image of Earth's subsurface. By doing this, we see the shape and can explore the origin of pit craters found offshore Australia that are ~148 million years-old and now buried several kilometres beneath the seabed. We show that some of the studied pit craters are connected to igneous dikes (solidified vertical sheets of molten rock) and others to faults (cracks in the rock). Our overall finding is that pit crater shape and size do not necessarily tell us much about the process(es) that formed them, or the properties of the material in which they formed.

## 1. Introduction

Quasi-circular topographic depressions are observed on the surface of Earth and many planetary bodies and asteroids (e.g., Abelson et al., 2003; Ferrill et al., 2004; Ferrill et al., 2011; Frumkin & Naor, 2019; Horstman & Melosh, 1989; Kling et al., 2021; Martin et al., 2017; Okubo & Martel, 1998; Sauro et al., 2020; Scott & Wilson, 2002; Whitten & Martin, 2019; Wyrick et al., 2004). These depressions, termed "pit craters", have diameters of meters to thousands of meters and are commonly arranged in linear chains (e.g., Kling et al., 2021; Whitten & Martin, 2019). The lack of raised rims and ejecta deposits around pit craters suggest they are not formed by bolide impacts (e.g., Halliday, 1998; Poppe et al., 2015; Wyrick et al., 2004). Instead, pit craters are thought to reflect the collapse of overlying rock and/or regolith into subsurface cavities or volumetrically depleted zones generated by (Figure 1) (see also Wyrick et al., 2004): (a) the dissolution of carbonate or salt (e.g., sinkholes; Abelson et al., 2003; Poppe et al., 2015; Spencer & Fanale, 1990); (b) release of overpressured fluids, perhaps due to faulting (e.g., pockmarks; Velayatham et al., 2019; Velayatham et al., 2018), which can
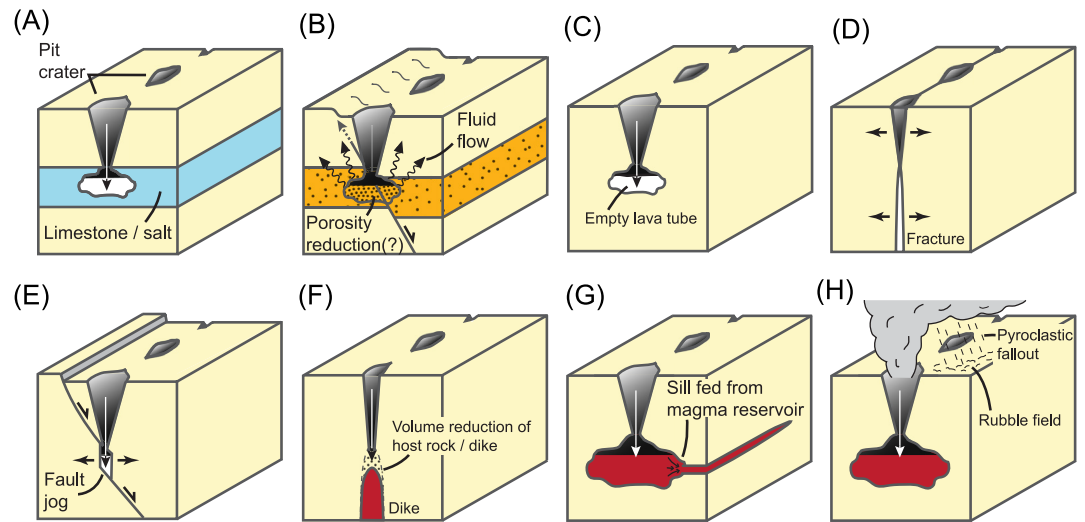
**Figure 1.** Conceptual models of pit crater formation (modified from Kettermann et al., 2019; Sauro et al., 2020; Velayatham et al., 2019; Velayatham et al., 2018; Wyrick et al., 2004). (a) Karst/salt dissolution. (b) Fluid flow. (c) Lava tube collapse. (d) Tensile fracturing. (e) Dilatational fault jogs. (f) Dike tip processes. (g) Magma migration. (h) Explosive volcanism.

locally reduce the porosity of the host material; (c) evacuation of lava tubes (see Sauro et al., 2020 and references therein); (d) opening of tensile fractures (e.g., Ferrill et al., 2011; Smart et al., 2011; Tanaka & Golombek, 1989); (e) local dilation where faults are steeply dipping (e.g., Ferrill et al., 2011; Ferrill & Morris, 2003; Ketterman et al., 2015; Kettermann et al., 2019; Smart et al., 2011; Von Hagke et al., 2019); (f) dike intrusion (e.g., Mège & Masson, 1996; Okubo & Martel, 1998; Scott & Wilson, 2002; Wall et al., 2010); (g) magma migration out of a reservoir (e.g., Mège et al., 2003; Poppe et al., 2015); and/or (h) explosive volcanism (e.g., Hughes et al., 2018).

If the surface expression of pit craters reflects their formation mechanism(s), we could use their morphology to interrogate inaccessible subsurface processes and structures on Earth, as well as other planetary bodies and asteroids (e.g., Kling et al., 2021; Korteniemi et al., 2010; Martin et al., 2017; Mège & Masson, 1997; Smart et al., 2011; Whitten & Martin, 2019). However, imaging pit craters on other worlds is difficult (Wyrick et al., 2004), and even our knowledge of the subsurface geometry of pit craters on Earth remains limited (cf. Abelson et al., 2003; Frumkin & Naor, 2019; Halliday, 1998; Wall et al., 2010). We thus rely on physical experiments and numerical modeling to predict how pit crater formation may translate into surface deformation (e.g., Hardy, 2021; Poppe et al., 2015; Smart et al., 2011). Identifying pit craters on Earth, the subsurface structure of which we *can* study, is crucial to validating these models and thus determining whether pit crater surface expressions can be used to distinguish formation mechanisms.

Reflection seismology provides unprecedented insight into Earth's subsurface and can uniquely resolve the three-dimensional structure of pit craters (Abelson et al., 2003; Magee et al., 2019; Magee & Jackson, 2020b; Wall et al., 2010). Here, we use seismic reflection data imaging part of a sedimentary basin, offshore NW Australia, to a conduct quantitative, 3D analysis of pit craters and their underlying structure. Seismic-stratigraphic analyses reveal that the now-buried pit craters developed during a phase of Late Jurassic igneous dyking (Magee & Jackson, 2020b). Our data allow us to: (a) quantify the palaeosurface expression and subsurface structure of pit craters in 3D; (b) identify underlying structures that may be related to pit crater formation; and (c) test whether the (palaeo)surface expression of pit craters are diagnostic of subsurface structure and processes.

We map 59 pit craters, which typically have a funnel-like appearance comprising an upper inverted cone that is underlain by a pipe, and are commonly arranged in linear chains. Most (54) pit craters occur in chains located along the floor of ≲2 km wide, buried graben that are bound by dike-induced faults and underlain by what were northwards-propagating dikes (Magee & Jackson, 2020b); five other pit craters are connected to steeply dipping portions of tectonic normal faults. The link between pit craters and dikes and faults confirms that magmatic processes and overburden collapse into dilatational fault jogs. By recognizing that some pit craters above dikes occur at different stratigraphic levels and broadly get younger southwards, we specifically suggest these pit craters may have formed when a waning of magma pressure and potential backflow led to a local volume reduction of

the dike. In addition to obtaining insight into pit crater formation mechanisms, we also show that pit crater depths are variable across the study area. Pit crater depth is one of the few morphological properties of pit craters that can be measured from surficial data, and has been suggested to provide a minimum estimate of regolith thickness on other planetary bodies (e.g., Whitten & Martin, 2019; Wyrick et al., 2004). The variability in pit crater depths we record suggest this characteristic may *not* always be controlled by regolith thickness. Overall, our work demonstrates that seismic reflection data provides a unique insight into the structure and growth of pit craters on Earth. Additional seismic-based studies will help us further understand extraterrestrial pit craters and, therefore, probe the subsurface structure and composition of other planetary bodies for which direct, in situ data are not yet available.

## 2. Geological Setting

The North Carnarvon Basin, offshore NW Australia (Figure 2a) formed during periodic rifting between Australia and Greater India in the Late Carboniferous-to-Early Cretaceous (e.g., Direen et al., 2008; Longley et al., 2002; Stagg et al., 2004). The Exmouth Plateau, where the studied pit craters are situated, lies within the North Carnarvon Basin and itself initially formed in a Rhaetian (Late Triassic) to Callovian (Middle Jurassic) rift phase, which produced an array of ~N-S-striking, normal faults with up to ~1 km of throw (Figure 2b) (e.g., Bilal et al., 2018; Black et al., 2017; Gartrell et al., 2016; Marshall & Lang, 2013; Stagg & Colwell, 1994; Tindale et al., 1998). These tectonic faults displace a thick pre-rift succession, including the fluvio-deltaic Mungaroo Formation, and accommodated deposition of a relatively condensed ($\lesssim$100 m thick), clastic-dominated, syn-rift succession (i.e., the Brigadier and North Rankin formations, the Murat Siltstone, and the Athol Formation; Figure 2b) (Hocking, 1992; Hocking et al., 1987; Stagg et al., 2004; Tindale et al., 1998).

The Callovian unconformity caps the Athol Formation and underlies the Oxfordian-to-Tithonian, marine Dingo Claystone, marking the end of a major period of Late Triassic-to-Middle Jurassic rifting (Figure 2b) (e.g., Tindale et al., 1998; Yang & Elders, 2016). Renewed rifting in the Tithonian (Late Jurassic) to Valanginian (Early Cretaceous) involved (Figure 2b): (a) sub-aerial development of the regionally mappable, Base Cretaceous unconformity at ~148 Ma (latest Tithonian); (b) rapid and substantial subsidence, which allowed deposition of the $\lesssim$3 km thick, fully marine Barrow Group; and (c) relatively limited upper crustal faulting, which was restricted to minor reactivation of older faults and the generation of an array of N-S to NE-SW striking, normal faults with throws typically <0.1 km (e.g., Driscoll & Karner, 1998; Magee et al., 2016; Paumard et al., 2018; Reeve et al., 2016). Continental break-up occurred along the western and southern margin of the Exmouth Plateau in the Valanginian-to-Hauterivian (~135–130 Ma; Figure 2b) (e.g., Direen et al., 2008; Reeve et al., 2021; Robb et al., 2005). Following break-up, thermal subsidence accommodated deposition of a thick post-rift succession that hosts several tiers of polygonal faults (e.g., Paganoni et al., 2019; Velayatham et al., 2019).

During the Late Jurassic, at ~148 Ma, a radial dike swarm, up to ~170–500 km long and ~300 km wide, was emplaced across much of the Exmouth Plateau (Figures 2a and 2b) (Magee & Jackson, 2020b). Associated with this dike swarm is an array of dike-induced faults that extend up from and dip toward the upper tips of dikes, offsetting Late Triassic-to-Late Jurassic strata and bounding dike-parallel graben (e.g., Figures 2c and 3a) (Magee & Jackson, 2020a, 2020b). Within these graben, linear chains of sub-circular depressions are recognised (e.g., Figures 2c and 3a) (Magee & Jackson, 2020b; Velayatham et al., 2018, 2019). These depressions, which are interpreted to have formed at the contemporaneous free surface, are underlain by pipe-like features that extend down toward dikes, dike-induced normal faults, or tectonic normal faults (e.g., Figures 2c and 3a) (Magee & Jackson, 2020b; Velayatham et al., 2018, 2019). The depressions have previously been interpreted as pockmarks formed by fluid escape from an over pressured horizon when faulting locally reduced the overburden pressure (e.g., Figure 1b) (Velayatham et al., 2018). However, the spatial and temporal association between the depressions and underlying dikes suggests that these landforms may be analogous to pit craters observed elsewhere on Earth and other planetary bodies (Magee & Jackson, 2020b); henceforth we refer to these depressions as "pit craters."

## 3. Data Set and Methods

The zero-phase, time-migrated Chandon 3D seismic reflection survey covers an area of ~951 km², has a bin spacing of 25 m, and a record length of 6 s two-way time (s TWT). We present seismic images where a trough (black) reflection has a positive polarity and corresponds to a downward increase in acoustic impedance, and a
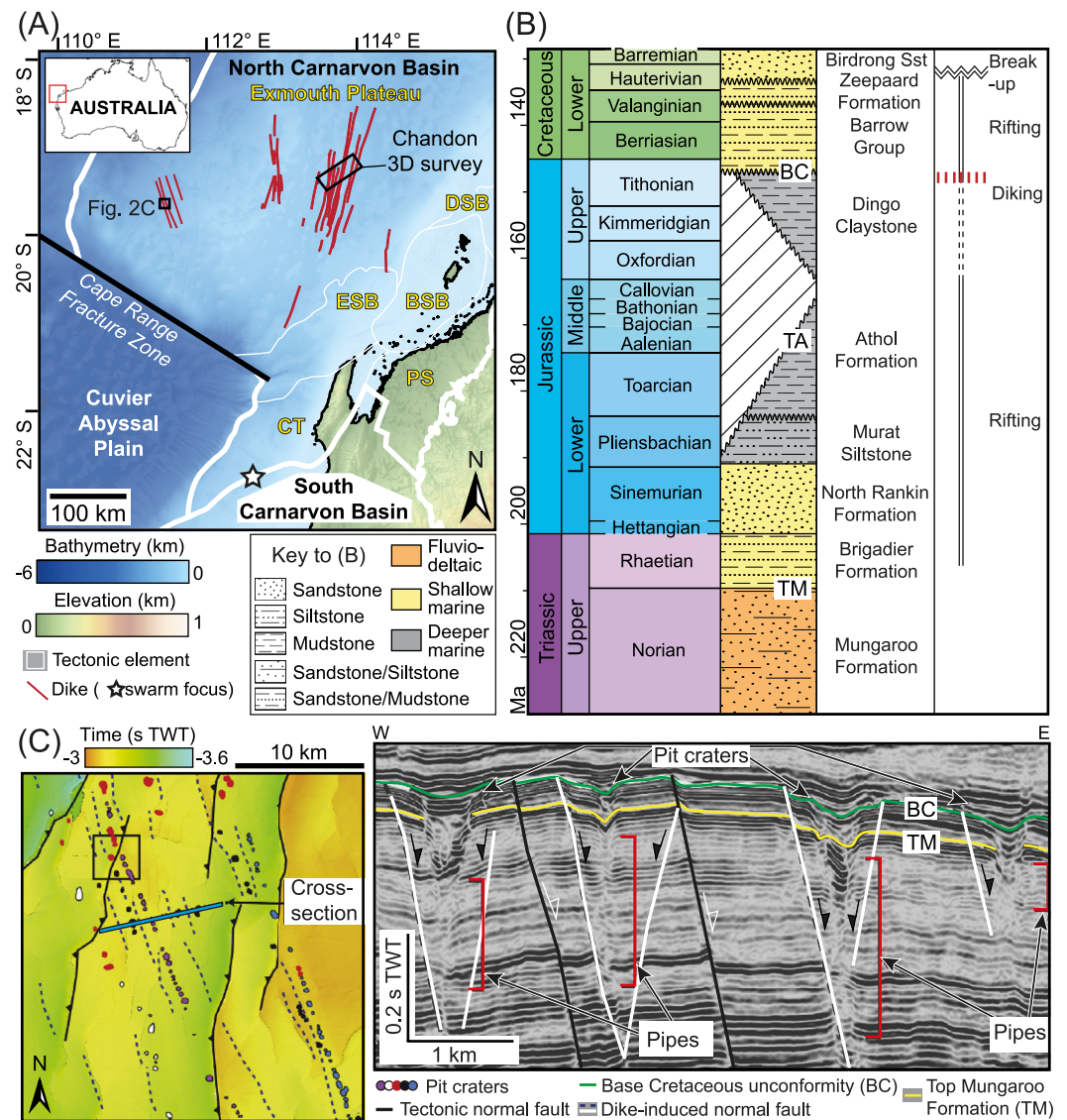
**Figure 2.** (a) Map of the southern portion of the North Carnarvon Basin highlighting principal tectonic elements, including the: ESB = Exmouth Sub-basin, CT = Carnarvon Terrace, BSB = Barrow Sub-basin, DSB = Dampier Sub-basin, and PS = Peedamullah Shelf. The location of the Exmouth Dike Swarm is also shown (Magee & Jackson, 2020b). Elevation data are based on the 2009 Australian Bathymetry and Topography grid (Geoscience Australia). Inset: Location map of the North Carnarvon Basin (NCB) relative to Australia. (b) Stratigraphic column for the Exmouth Plateau summarizing the age, dominant lithology, and generalized depositional environment for key units (after Hocking et al., 1987; Partington et al., 2003; Tindale et al., 1998). Key tectonics and magmatic events are also shown for (see Reeve et al., 2021 and references therein). (c) Interpreted time-structure map and seismic section showing pit crater-like features arranged in chains and associated with normal faults in the western portion of the Exmouth Plateau (modified from Velayatham et al., 2018). See Figure 2a for map location.

peak (white) reflection has a negative polarity and represents a downward decrease in acoustic impedance (e.g., Figure 3a). To help identify and map the pit craters, their underlying dikes, and spatially associated faults, we extract a variance volume attribute; this parameter accentuates spatial variations in waveform similarity, which may relate to and so reveal these geological features (e.g., Chopra & Marfurt, 2005; Marfurt & Alves, 2015).

We use data from five local boreholes (Chandon-1, Chandon-2, Chandon-3, Mercury-1, and Yellowglen-1) to establish estimates for: (a) the age and intervening lithology of three mapped stratigraphic horizons, which correspond to the Top Mungaroo Formation (TM; ~209 Ma), Top Athol Formation (TA; ~164 Ma), and Base Cretaceous unconformity (BC; ~148 Ma); (b) an average time-depth relationship for the subsurface (see Supporting
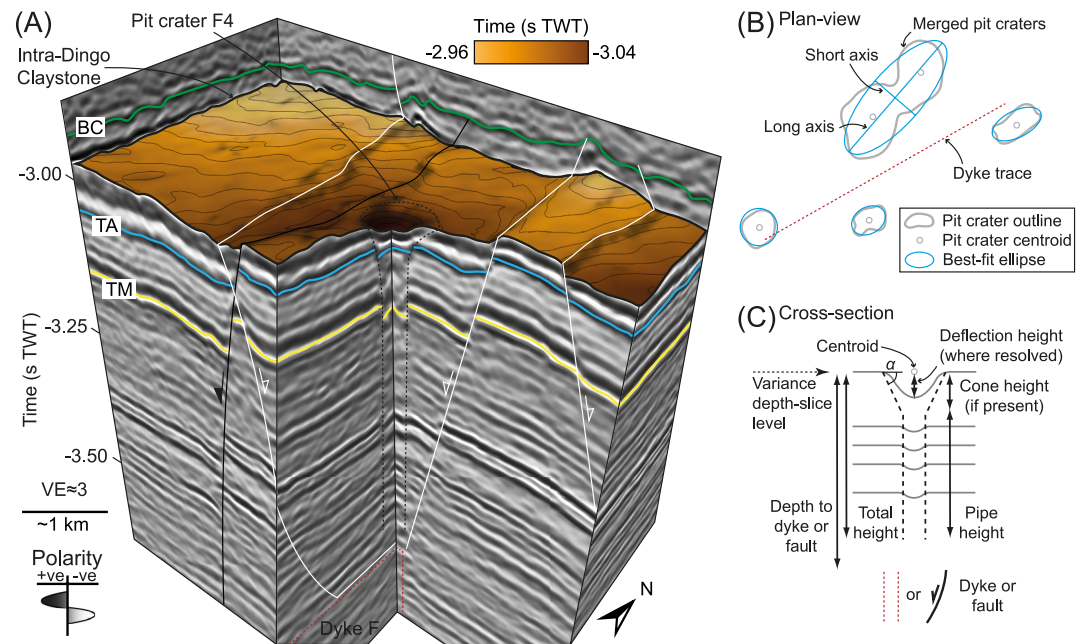
**Figure 3.** (a) 3D view of a funnel-like pit crater (F4), the top of which occurs at a horizon between the Base Cretaceous unconformity (BC) and Top Athol Formation (TA) (Magee & Jackson, 2020b). This pit crater occurs within a graben and extends down to the top of Dike F, below the Top Mungaroo Formation (TM). (b) and (c) Schematics showing the measurements of pit crater plan-view (b) and cross-sectional (c) morphologies.

Figure 1), allowing us to depth-convert (from ms TWT to meters) measurements taken from the top 4 s TWT of the survey; and (c) the seismic velocity ($v$) range of the interval of interest within which the pit craters are imaged. Seismic velocity increases with depth, from 2.64($\pm$10%) to 3.66($\pm$10%) km s$^{-1}$, as the dominant frequency ($f$) of the data broadly decreases from ~33 to ~23 Hz; with this information we calculate the wavelength ($\lambda = v/f$) of the seismic data, estimating that its vertical seismic resolution can be characterized by limits of separability ($\lambda/4$) of 37($\pm$7)–17($\pm$3) m and limits of visibility ($\lambda/30$) of 5($\pm$1)–3($\pm$1) m (e.g., Brown, 2011). The limits of separability and visibility correspond to the minimum vertical distance between two features required for them to be imaged, respectively, as: (a) two discrete reflections; and (b) a tuned reflection package, created by the convolution of the two reflections on their return to the surface (Brown, 2011). The horizontal resolution of the time-migrated seismic reflection data is estimated to be at least 25 m, which is equivalent to the bin spacing, and likely increases to 37($\pm$7) m (i.e., $\lambda/4$) with depth.

### 3.1. Plan-View Measurements

We identify 59 pit craters, some of which occur in chains overlying nine dikes that we label Dike A to Dike I (Magee & Jackson, 2020a, 2020b); depending on the underlying dike, we label these pit craters A$n$ to I$n$ if they overlie a dike. There are a few pit craters spatially related to tectonic normal faults and we label these X$n$. For both dike- and tectonic fault-related pit craters, $n$ denotes the pit crater number, which increases along each chain from south to north. We map the plan-view outline of each pit crater at: (a) their uppermost expression in the seismic reflection data, which varies stratigraphically depending on location within the basin; and (b) where pits intersect the stratigraphically deeper, Top Athol Formation. Our approach allows us to characterize how pit crater plan-view morphology changes with depth. For each mapped pit crater outline, we use image analysis software (ImageJ) to define a best-fit ellipse and centroid position (Figure 3b); for each centroid position, we extract its $X$, $Y$, and $Z$ co-ordinates. Where pit craters appear to have merged, we define an encompassing best-fit ellipse but manually determine centroid positions (Figure 3b). We use the outline of each pit crater, or merged pit craters, to measure pit area and use the best-fit ellipses to determine pit long axis lengths and azimuths, as well as short axis lengths (Figure 3b). From these values, we calculate the plan-view aspect ratio of the pit crater planform shape. By using these parameters to define the plan-view morphology of the studied pit craters, we can compare them to the surface expression of pits elsewhere (e.g., Kling et al., 2021; Whitten & Martin, 2019), and assess

any relationship between their geometry and subsurface structures and/or stresses (e.g., Magee & Jackson, 2020b; Paulsen & Wilson, 2010).

### 3.2. Cross-Section Measurements

The only cross-section attributes commonly available to measure for most pit craters on Earth and other planetary bodies are their depth and slope; together, these parameters can be used to estimate pit volume (e.g., Gwinner et al., 2012; Sauro et al., 2020; Scott & Wilson, 2002; Wyrick et al., 2004). Most pit craters we study (54; i.e., 92%) display a funnel-like morphology comprising an upper, inwardly inclined conical surface, which we refer to as an "inverted cone", underlain by a sub-vertical cylindrical "pipe" (e.g., Figure 3a). Some pit craters lack an inverted cone, and so we refer to their morphology as pipe-like. Stratigraphic reflections within many of the inverted cone sections appear continuous with the flanking host rock, although these intra-pit reflections are often locally deflected downwards (e.g., Figure 3c). Note that for some pit craters it is difficult to correlate internal and external stratigraphic reflections. Where possible, we measure both the maximum "cone height" and "deflection height" of pit craters (Figure 3c), to test which, if either, is equivalent to pit crater depths presented in other studies. Cone height and deflection height are specifically measured relative to the position of the pit crater centroid Z co-ordinate, which marks the palaeosurface location of the pit crater site (Figure 3c).

By integrating these measurements with those of pit crater long axis lengths, we estimate slopes and volumes of the inverted cone sections and deflected reflections, under the assumption that pits have a simple elliptical plan-view morphology (Figure 3c) (Wyrick et al., 2004). We also measure "pipe height", which for funnel-like pit craters we define as the vertical distance from the base of the inverted cones to where the pit crater structure is no longer seismically resolved (Figure 3c). We calculate pipe volume from the pipe height and the pit crater long axis length as measured at the Top Athol Formation. To aid comparison between pit craters with and without a funnel-like morphology, we describe each as having a "total height"; for pipe-like pit craters their total height is equal to pipe height, but for funnel-like pit craters their total height includes the cone height and pipe height (e.g., Figure 3c). Our measured pipe and total heights are minimum estimates, as a reduction in imaging with depth and the presence of other structures (e.g., faults), can limit our ability to determine the true base of pit craters (Velayatham et al., 2018, 2019; Wall et al., 2010). We also measure the depth of dikes or normal faults directly beneath the top of each pit crater (Figure 3c).

### 3.3. Sources of Error

The pit craters we study here are buried within a sedimentary basin. As basins subside and sediment load is added, buried rocks will compact (e.g., Sclater & Christie, 1980). Such burial-related compaction can reduce the dip of inclined surfaces and decrease the vertical height of structures; that is, our measurements of deflection height, cone height, cone slope, and pipe height should thus be considered minimum estimates. Another primary error source in our study relates to uncertainty in the seismic velocities used to depth-convert the seismic data from seconds two-way time to depth in meters. For example, our depth conversion assumes that seismic velocities do not vary laterally across the study area away from the boreholes where we obtain velocity data from. Although the similarity in the time-depth relationships for all four boreholes wells within the Chandon 3D survey supports our assumption that there is little lateral variation in seismic velocity (Figure S1 in Supporting Information S1), we conservatively consider that calculated velocities and measured dominant frequencies may differ by up to $\pm10\%$ (Magee & Jackson, 2020b). Measurements of limits of separability and visibility, deflection height, cone height, pipe height, and the depth to underlying dikes thus have assumed depth conversion-related errors of $\pm10\%$. Manual mapping and measurement can also introduce human errors (e.g., in defining pit crater pipe bases) that cannot be quantified. For example, we cannot definitively constrain the true positions of pit crater outlines due to data horizontal resolution. In an attempt to account for human error, we consider these errors may be up to $\pm5\%$ (Magee & Jackson, 2020b). Overall, plan-view measurements are presented with $\pm5\%$ errors as they are susceptible to human error and limitations in spatial positioning due to the horizontal resolution of the seismic data, but are not associated with errors arising due to uncertainties in subsurface velocities and depth-conversion. For measurements of pit height, cone height, pipe height, and the depth to underlying dikes, we estimate cumulative errors of $\pm15\%$; this estimate is based on the uncertainties in the calculated seismic velocities and potential human measurement errors.

## 4. Results

### 4.1. Stratigraphic and Structural Framework

Stratigraphic reflections within the interval of interest typically have a moderate amplitude and laterally continuous character (Figure 4a). In places these reflections are: (a) offset by ∼N-S-striking, linear-to-curvilinear, moderate-to-high throw (up to ∼500 m) tectonic normal faults (e.g., Figures 4a–4d); (b) cross-cut by sub-vertical, ∼N-trending dikes (named A to I) that are expressed as >100 m wide zones of disrupted, low-amplitude reflections (Figures 4a and 4e); (c) displaced by graben-bounding, low-throw (≲0.1 km), dike-induced normal faults that dip toward and converge upon the upper tips of the underlying dikes at depths of ∼3–3.5 km (Figure 4a); or (d) intersected by pit craters (see below) (Figures 3 and 4a). Below the Base Cretaceous unconformity, pit craters and dikes are marked by a high variance attribute value, as are areas where strata are folded and/or offset by tectonic faults (e.g., Figure 4a).

### 4.2. Pit Crater Morphology

Pit craters ($n = 59$) occur across the data set, primarily arranged in chains aligned parallel to and occurring within dike-induced graben (Figure 5a). Five pit craters (*X1–X5*) are located outside these graben and are instead situated in the hanging wall of tectonic normal faults (Figure 5). Of the 54 pit craters within dike-induced graben, 50 have a funnel-like morphology in cross-section, as do four of the pit craters associated with tectonic normal faults (Figures 5–7). The remaining four pit craters within dike-induced graben (A4, F5, G7, and H1), as well as *X3*, have a pipe-like geometry and no inverted cone section (Figures 5–7).

At the Top Athol Formation, we mapped 61 pit crater pipes (Figure 5b), which is greater than the 59 pit craters we define at shallower stratigraphic levels because three pipes merge upwards (E1a and b, F10a and b, G10a and b) and an additional pipe splits (G2/3) above the Top Athol Formation (Figure 6). Of the 57 pit crater pipes within dike-induced graben at the Top Athol Formation, 30 occur directly above dike traces and the rest are situated ∼75–653 m orthogonally from the associated dike trace (Figure 5b). The only pipe-like pit crater located directly above a dike trace is A4 (Figure 5).

#### 4.2.1. Plan-View Geometry

Within dike-induced graben, funnel-like pit crater tops have long axes of 150–740 m, areas of 0.05–1.24 km$^2$, and are quasi-circular to elliptical with aspect ratios of 1.04–3.05 (Figures 5 and 8a; Table S1 in Supporting Information S1). The orientations of these pit crater long axes are variable, with a mean axis trend of 080° and a mode of 005–015° (Figure 5c). At the Top Athol Formation, typically located below inverted cone sections, the pipes of these funnel-like pit craters are smaller in plan-view: long axis lengths are 108–585 m, aspect ratios are 1.01–3.14, and areas are 0.02–0.10 km$^2$ (Figures 5b and 8a, and c; Table S1 in Supporting Information S1). For pipe-like pit craters within dike-induced graben, their plan-view outlines at their tops are characterized by long axes of 170–390 m with no clear preferred alignment, aspect ratios of 1.23–1.63, and areas of 0.06–0.39 km$^2$ (Figures 5 and 8a; Table S1 in Supporting Information S1). At the Top Athol Formation, pipe-like pit crater long axes within dike-induced graben are 117–364 m, have aspect ratios of 1.22–1.47, and areas of 0.04–0.32 km$^2$ (Figures 5b and 8a; Table S1 in Supporting Information S1).

The area and aspect ratio of the 29 pit craters situated directly above dikes broadly decrease ($R^2 = 0.55$) and seemingly increase ($R^2 = 0.29$), respectively, with depth, and tend to be larger than those above dike-induced faults (Figure 8b). Although the 29 pit craters above dikes cumulatively have a mean long axis orientation of 077°, six are oriented between 005 and 015°, sub-parallel to the mean axis (011°) of dike segments in the study area (Figure 5c). The size and shape of the 25 pit craters above dike-induced faults varies non-systematically with depth; that is, the correlation between area and aspect ratios measured at the pit crater tops and at the structurally deeper Top Athol Formation are $R^2 = 0.26$ and $R^2 = 0.08$, respectively (Figure 8b).

Pit craters with a funnel-like morphology, but associated with tectonic normal faults (*X1*, *X2*, *X4*, and *X5*), are typically larger than those within dike-induced graben and have long axes of 400–740 m, aspect ratios of 1.17–1.55, and areas of 0.33–1.47 km$^2$ at their tops (Figures 5 and 8a; Table S1 in Supporting Information S1). At the Top Athol Formation, these funnel-like pit craters have long axes of 358–790 m, aspect ratios of 1.10–2.24, and areas of 0.18–1.66 km$^2$ (Figures 5b and 8a; Table S1 in Supporting Information S1). The only pit crater associated with a tectonic normal fault that does not have a funnel-like morphology, *X3*, is 140 m long, has an aspect ratio
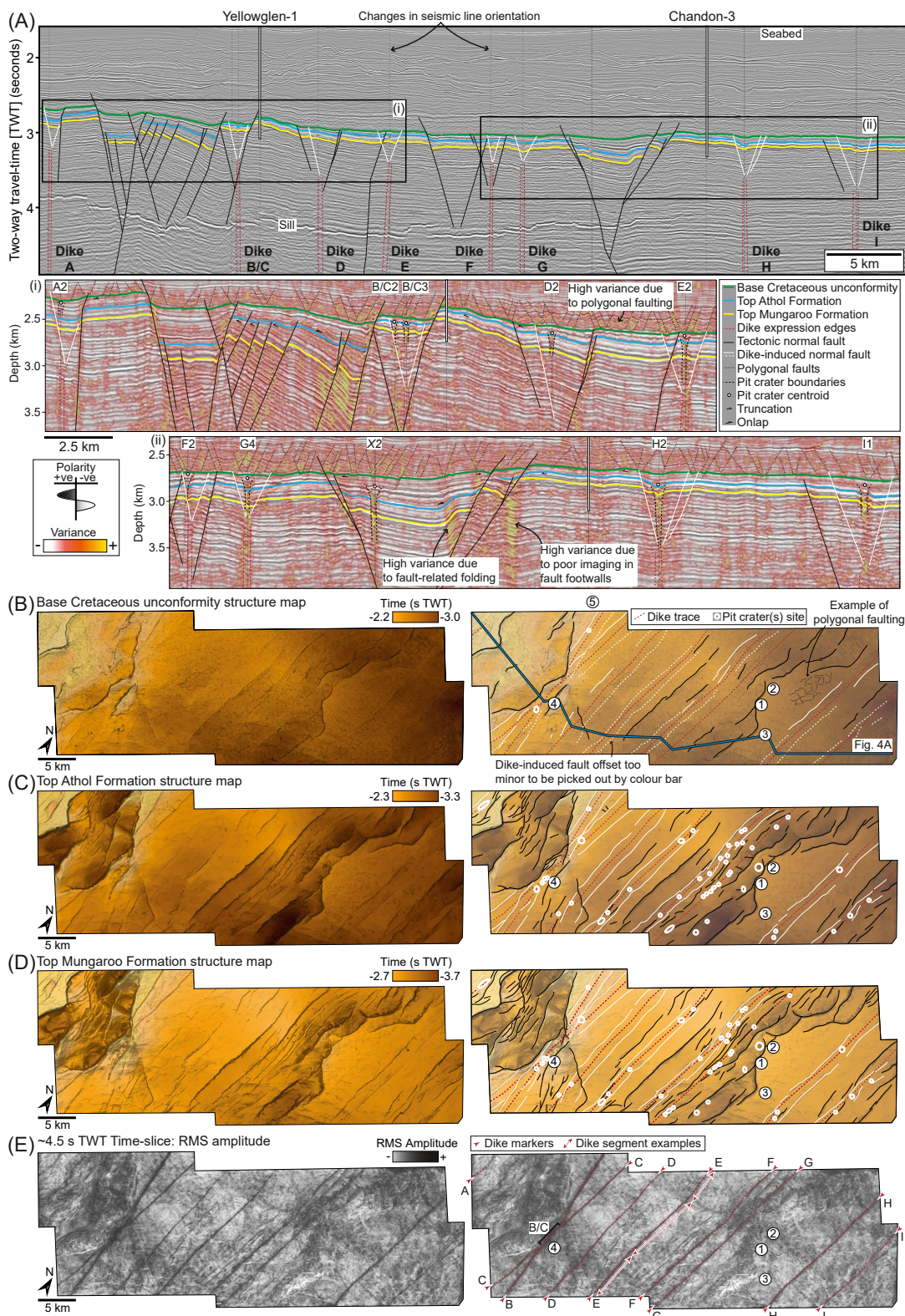
**Figure 4.**
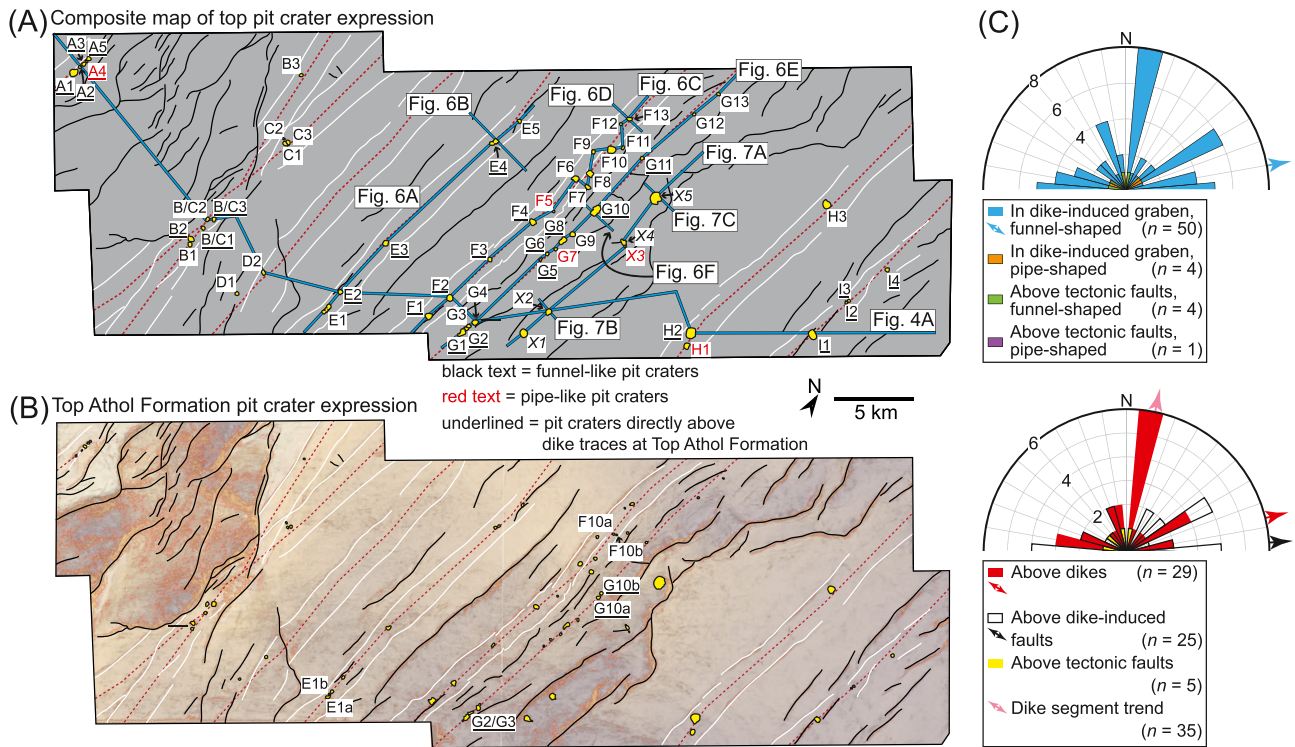
**Figure 5.** (a) Composite map showing the outlines of each pit crater at the shallowest stratigraphic level at which they occur, relative to dike and fault traces. (b) Map showing the expression of each pit crater at the Top Athol Formation. See Figure 4a for key. (c) Rose plots showing the orientation of pit crater long axes, grouped by pit crater morphology and/or association with different structures (Table S1 in Supporting Information S1). Arrows show the mean vector of select populations. The orientations of dike segments are also shown (Magee & Jackson, 2020b).

of 1.3, and an area of 0.05 km² at its top (Figure 8a; Table S1 in Supporting Information S1). At the Top Athol Formation, this pipe-like pit crater is 98 m long, has an aspect ratio of 1.6, and an area of 0.02 km² (Figure 8a; Table S1 in Supporting Information S1). Of the pit craters above tectonic faults, some increase in area or aspect ratio with depth, whereas others decrease (Figure 8b). There is no preferred orientation of pit crater long axes above tectonic faults (Figure 5c).

### 4.2.2. Cross-Section Geometry

In cross-section, pit crater walls typically bound zones within which stratigraphic reflections locally have a lower amplitude and are deflected (e.g., E4b) or are displaced (e.g., F13) downwards relative to those in the flanking host rock (Figures 4a, 6, and 7). Pit crater centroids are typically situated within the Dingo Claystone, ~16–188 m (i.e., 0.5–5.5 seismic reflection pairs where one pair comprises a peak and trough reflection) beneath the Base Cretaceous unconformity (Figures 4a, 6, 7, 9a, and 9b). Only B1-B3 and D1-D2 are expressed at the Base Cretaceous unconformity (Figure 9a; Figure S2 in Supporting Information S1). Stratigraphic reflections overlying some pit craters appear locally thickened (e.g., F13; Figure 6d), whereas others seem to onlap onto the corresponding crater walls (e.g., G10a; Figure 6f).

For each pit crater chain situated within dike-induced graben, the depth of their pit crater centroids beneath the Base Cretaceous unconformity vary by ≲60 m along their length (Figure 9a). Several pit crater chains (A, F, G,

**Figure 4.** (a) Interpreted composite section capturing the tectono-stratigraphy of the area, intersecting all dikes (a)–(i) and revealing the structure of some dike-induced normal faults and pit craters. The line also intersects the Yellowglen-1 and Chandon-3 boreholes. The time-migrated data are shown in the top panel, and in the lower panels we show selected depth-converted reflectivity data overlain by a variance attribute. See Figure 4b for seismic line location. (b)–(d) Time-structure maps of the three major horizons (Base Cretaceous unconformity, Top Athol Formation, and Top Mungaroo Formation) interpreted in Figure 4a. Uninterpreted and interpreted versions of the maps are shown, highlighting underlying dike traces, faults, and boreholes. The boreholes shown are: 1 = Chandon-1; 2 = Chandon-2; 3 = Chandon-3; 4 = Yellowglen-1; and 5 = Mercury-1. (e) Uninterpreted and interpreted RMS (root-mean squared) amplitude time-slice at 4.5 s two-way time (TWT) showing the seismic expression of dikes a–i. For part of their length, dikes b and c merge and we cannot determine if both dikes are continuous, or if one cross-cuts and displaces the other.
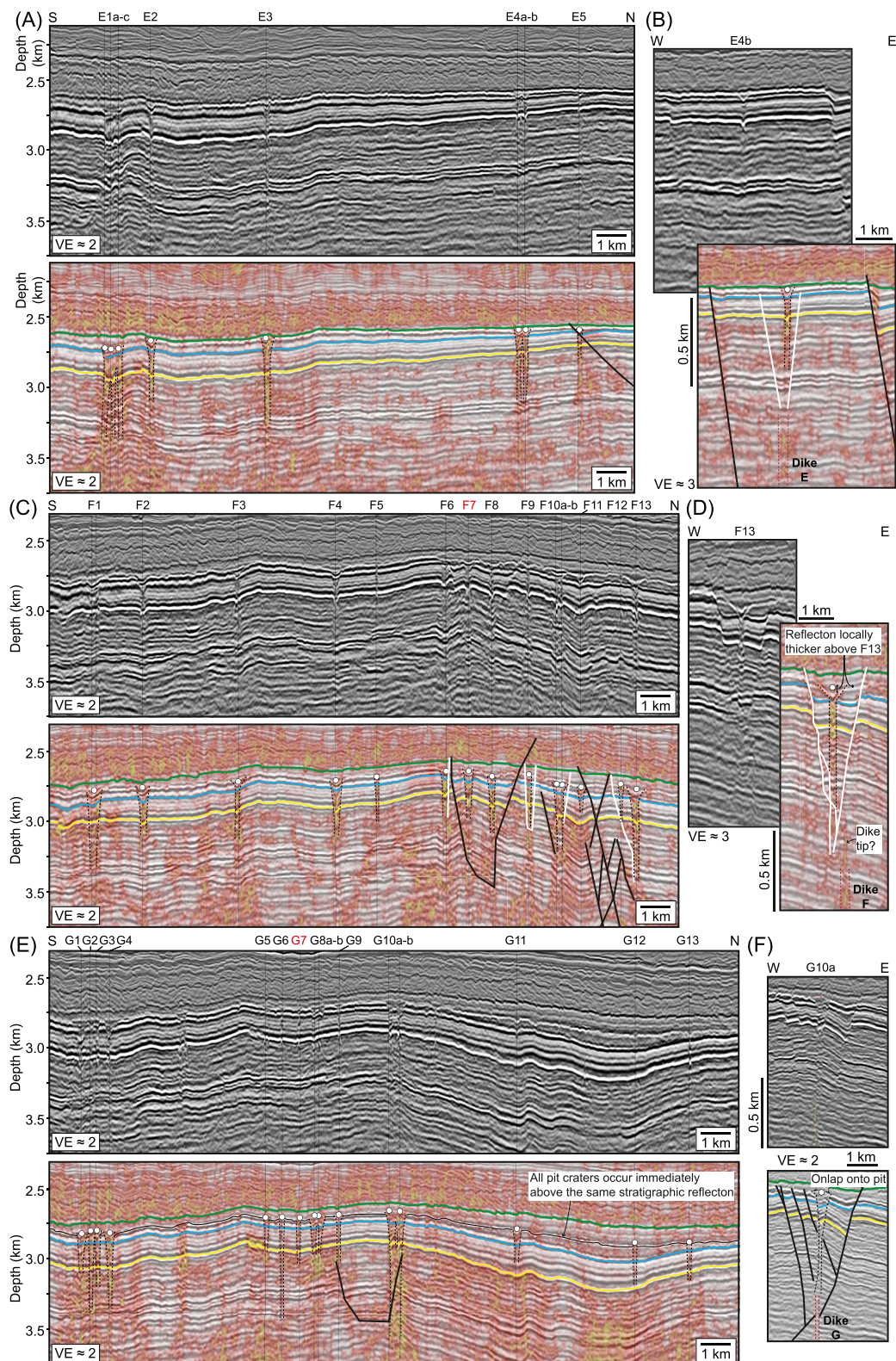
**Figure 6.**
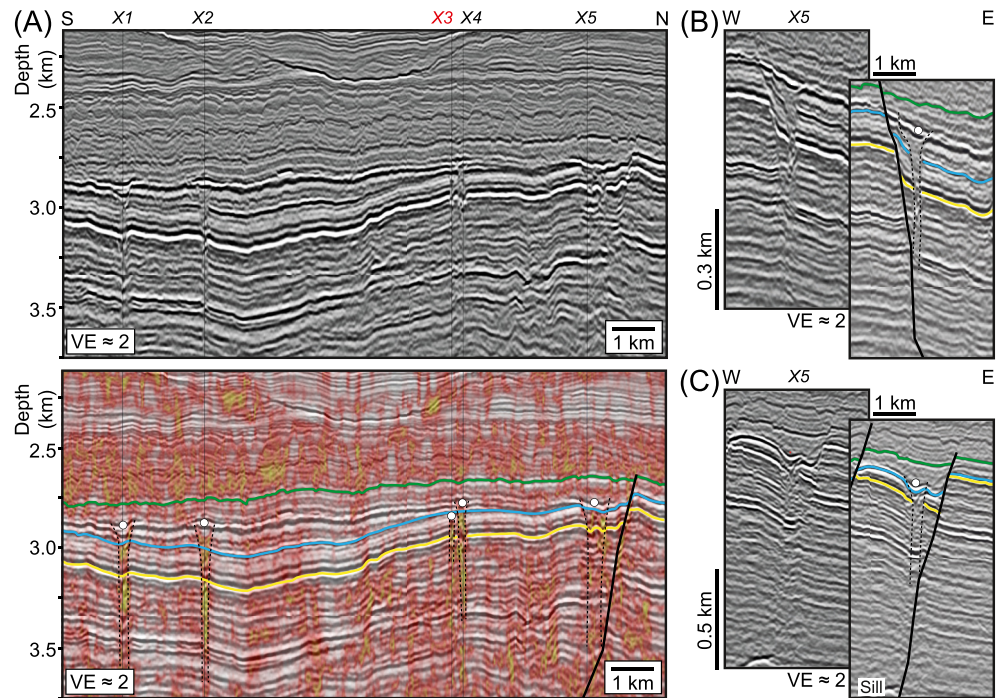
**Figure 7.** (a–c) Uninterpreted and interpreted, depth-converted seismic sections showing the structure of pit craters (X1-X5) associated with tectonic normal faults. The large section (a) is oriented sub-parallel to the pit chains imaged, whereas the small panels (b and c) are seismic sections oriented orthogonal to the pit chain trend. Pits labeled in black have a funnel-like geometry in cross-section, whereas those in red are pipe-like. See Figure 4 for interpreted section key and Figure 5a for seismic line locations.

and I) show a broad northwards increase in centroid depth (Figure 9a). Above some dikes, pit crater centroids all occur along the same stratigraphic reflection (i.e., D and G), even though the number of seismic reflection pairs between their level and the Base Cretaceous unconformity may differ (i.e., the post-overburden changes in thickness over a length-scale greater than that of an individual crater or chain of craters) (Figures 6c and 9b; Figure S2d in Supporting Information S1). For other chains, pit crater centroids coincide with different (deeper or shallower) reflections along their length (i.e., A, B, C, E, F, H, and I) (Figures 6 and 9b; Figure S2 in Supporting Information S1). The pit craters associated with tectonic normal faults have centroids that occur at the same stratigraphic reflection above the Top Athol Formation, except for *X3* which is the only pit crater to terminate below the Top Athol Formation (Figure 7).

Where pit craters display a funnel-like morphology, we measure the height of their inverted cone section and occasionally the deflection of the uppermost stratigraphic reflection within them (i.e., the deflection height) (Figure 3b). We find that inverted cone heights are ~18–245 m, with slopes of 7–51°, and that these values change across the study area and along individual pit crater chains (Figures 9c, 10a, and 10b; Table S1 in Supporting Information S1). The corresponding pipe heights of these funnel-like pit craters are 27–789 m (Figure 10a; Table S1 in Supporting Information S1); the heights of pipe-like pit craters are 107–254 m (Table S1 in Supporting Information S1). There is no correlation between cone height and total height or pipe height for pit craters within dike-induced graben (either those above dikes or dike-induced faults), or for those associated with tectonic normal faults (Figures 10a and 10b; Table S1 in Supporting Information S1). Deflection heights are ~4–21 m, with slopes <12°, and do not correlate with either total height or cone height (Figures 10c and 10d; Table S1 in Supporting Information S1).

**Figure 6.** (a)–(f) Uninterpreted and interpreted, depth-converted seismic sections showing the structure of pit craters associated with selected dikes e, f, and g The large sections (a, c, and e) are oriented sub-parallel to the pit chains imaged, whereas the small panels (b, d, and f) are seismic sections oriented orthogonal to the pit chain trend. Because of the relative orientation of the seismic lines presented and that of some non-planar tectonic faults they intersect, in places the faults appear have "V-" or "U-shaped" geometries. Pits labeled in black have a funnel-like geometry in cross-section, whereas those in red are pipe-like. See Figure 4 for interpreted section key and Figure 5a for seismic line locations. VE = vertical exaggeration.
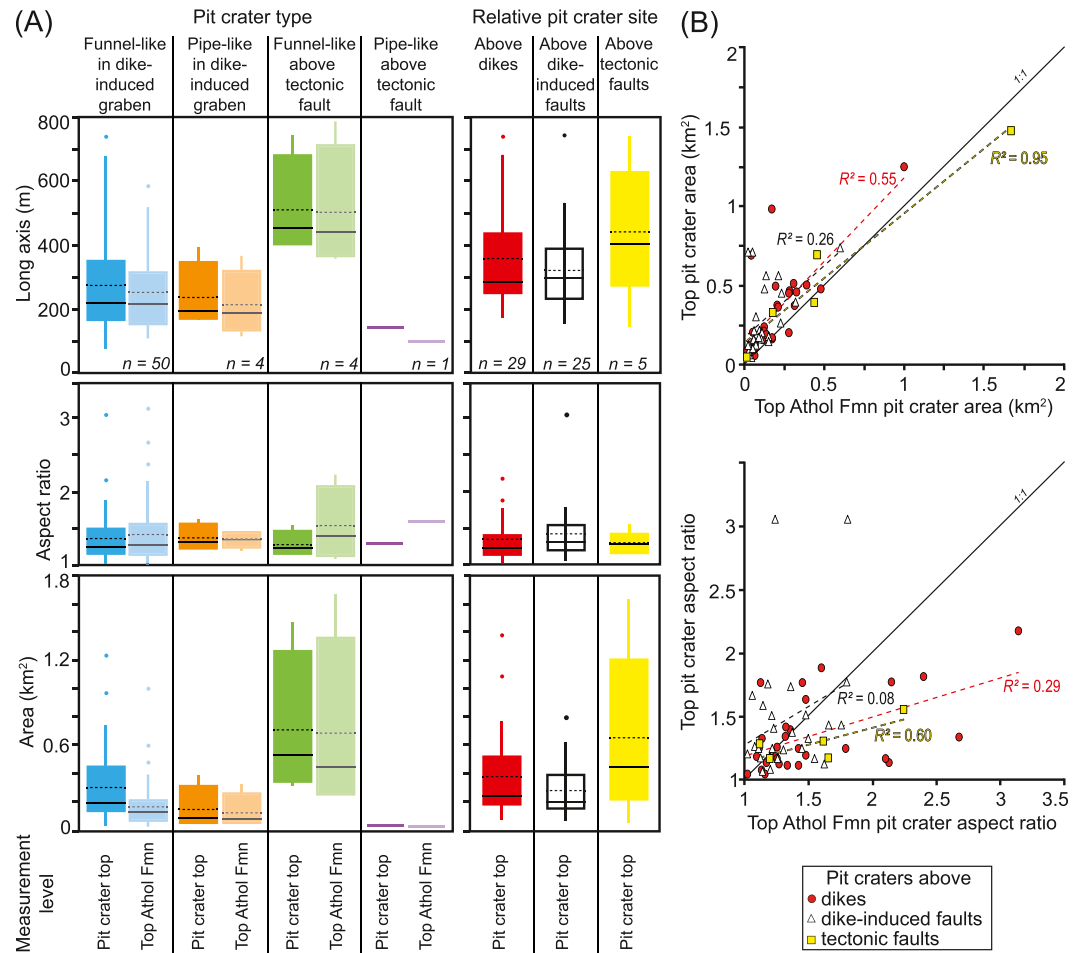
**Figure 8.** (a) Box-and-whisker plots comparing the long axes, aspect ratios, and areas of pit craters measured at two stratigraphic levels, distinguishing those that have different geometries (i.e., funnel-like and pipe-like) and/or associated with different structures (i.e., dikes, dike-induced faults, and tectonic faults) (Table S1 in Supporting Information S1). Here $n$ = number. The plots also highlight data median (thin black line), mean (dashed black line), and outliers in these data. See Figure 3b for an explanation of measured parameters. (b) Graphs comparing the area and aspect ratio of pit crater expressions at their tops and at the Top Athol Formation, grouping the data based on whether they are located directly above dikes, dike-induced faults, and tectonic faults.

Although the total heights of the pit craters are not consistent across the data, with most extending down into the Mungaroo Formation (Figures 4a, 6, and 7); pit craters G5, G11, and G12 appear to terminate at or above the Top Mungaroo Formation (Figure 6e). In places, mapped bases of pit crater pipes coincide with the upper tips of underlying dikes (G2, G4, G6, G10a, G12, and H2) or dike-induced fault planes (B/C2, C2, C3, F9, F13, I2, and I3) (Figure 6; Figure S2 in Supporting Information S1). The *X1-X5* pit crater pipes all extend down to tectonic faults (e.g., Figure 7). Where the base of pit crater pipes intersect dike-induced or tectonic faults, they often do so where the fault planes are relatively steep or sub-vertical (e.g., Figures 6b and 6d). Other pit craters appear to terminate within strata overlying dike upper tips or fault planes (Figures 4a, 6, and 7). Our measurements show pit crater total height ranges 114–868 m (Table S1 in Supporting Information S1). Between pit crater total heights and long axis lengths there is a weak but positive correlation for pits above dikes ($R^2 = 0.17$), no meaningful correlation for pit craters above dike-induced faults ($R^2 = 0.04$), but a strong positive correlation for those above tectonic faults ($R^2 = 0.71$) (Figure 11a). Visually similar pit craters recognised elsewhere across the Exmouth Plateau within dike-induced graben (e.g., Figure 2c) display a moderate ($R^2 = 0.37$–$0.50$) positive correlation between total height and long axes (Figure 11a) (see Velayatham et al., 2019). For all measured pit craters across the Exmouth Plateau there is no correlation ($R^2 \leq 0.06$) between total height and the aspect ratio of their long and short axes (Figure 11b).
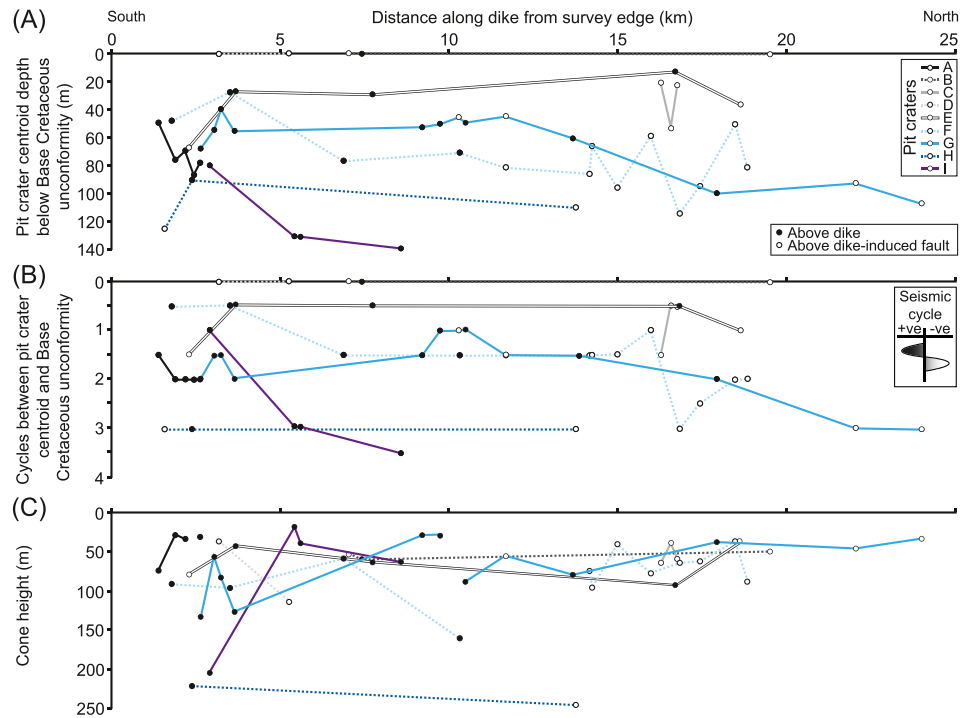
**Figure 9.** (a) and (b) Plots showing the depth (a) or number of seismic reflection pairs (b) that pit crater centroids are found beneath the Base Cretaceous unconformity along dike-strike (Table S1 in Supporting Information S1). Inset into (b): schematic depicting what constitutes a seismic reflection pair. (c) Plot of cone height along dike strike (Table S1 in Supporting Information S1). See Figure 3b for an explanation of measured parameters.

### 4.2.3. Comparative Analyses

For pit craters above dikes, dike-induced faults, and tectonic faults, there are relatively weak to relatively strong positive, power-law correlations between cone height and pit crater long axes, although not all correlations are equally robust ($R^2$ values are 0.61, 0.24, and 0.77, respectively; Figure 11). These trends are consistent with power-law correlations that define pit crater depth and long axes of craters observed elsewhere on Earth and on other planetary bodies (Figure 11) (e.g., Ferrill et al., 2011; Gwinner et al., 2012; Okubo & Martel, 1998; Scott & Wilson, 2002; Whitten & Martin, 2019; Wyrick et al., 2004). There is no correlation ($<R^2 = 0.08$) between deflection height and pit crater long axes (Figure 11). Inverted cone volumes ($1.10 \times 10^{-4}$ km$^3$ to $2.31 \times 10^{-2}$ km$^3$), and those of the deflected reflections ($7.36 \times 10^{-5}$ km$^3$ to $1.38 \times 10^{-3}$ km$^3$), are typically smaller than corresponding pipe volumes ($1.41 \times 10^{-3}$ km$^3$ to $2.79 \times 10^{-1}$ km$^3$) (Table S1 in Supporting Information S1).

## 5. Discussion

### 5.1. Pit Crater Formation

#### 5.1.1. Pit Crater Structure

Seismic reflection data provide unique opportunities to image and quantify the full 3D geometry of pit craters. Like pit craters observed elsewhere on Earth and other planetary bodies, those on the Exmouth Plateau have manifest as quasi-circular depressions, which in plan-view are commonly arranged in chains (e.g., Figures 3a and 5). Offsets of stratigraphic unit reflections within most mapped pit craters indicate that these structures form because of spatially restricted host rock subsidence (Figures 3a, 4a, 6, and 7). This subsidence is confined to cylindrical pipe-like structures with sub-vertical walls, which toward their tops commonly widen and become inwardly inclined, broadly describing an inverted conical shape (i.e., they are funnel-like) (Figures 3a, 4a, 6, and 7). These observations are consistent with the inferred subsurface geometry of pit craters recognised elsewhere and those modeled using physical or numerical approaches (e.g., Ferrill et al., 2011; Kettermann et al., 2019; Wyrick, 2004; Wyrick et al., 2015).
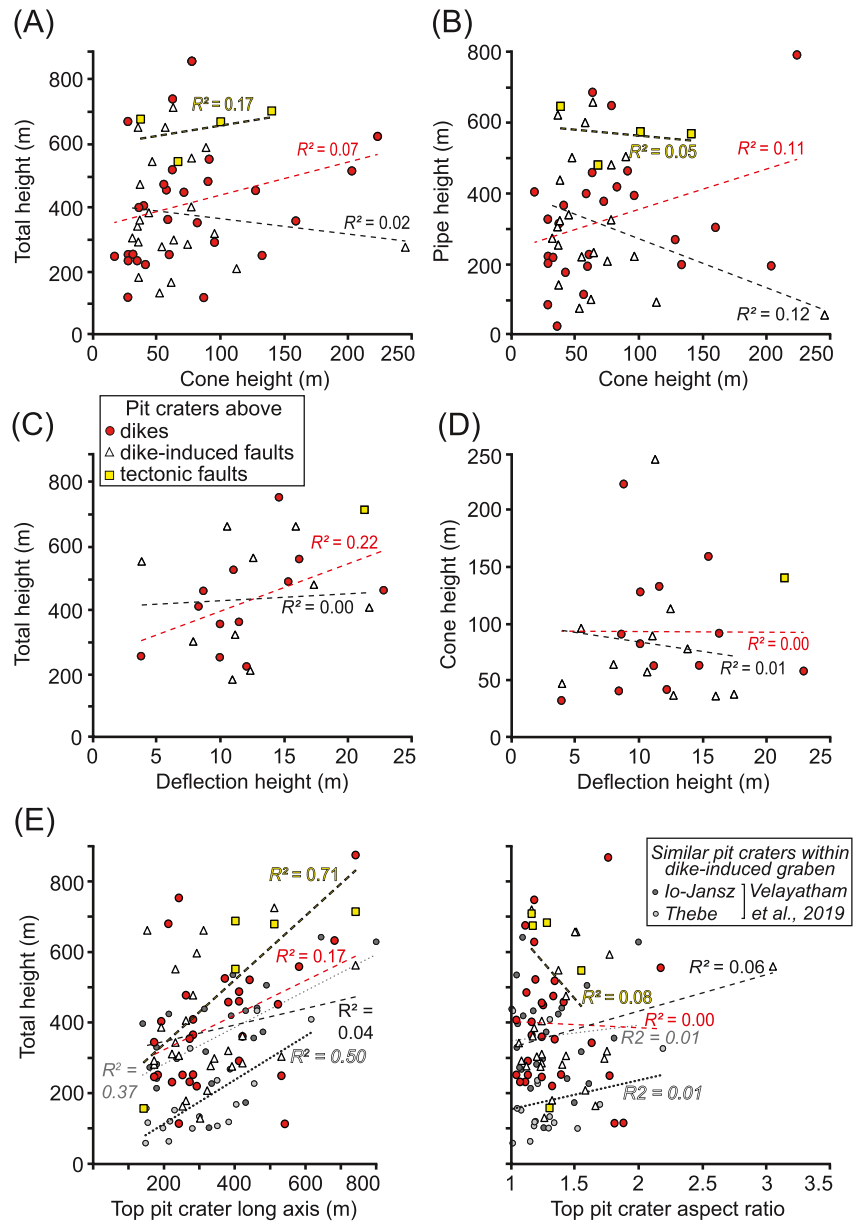
**Figure 10.** (a–d) Graphs comparing how the total height, pipe height, cone height, and deflection height are related (Table S1 in Supporting Information S1). See Figure 3b for an explanation of measured parameters. (e) Plots comparing total height to pit crater long axes and aspect ratio for those located above dikes, dike-induced faults, and tectonic faults (Table S1 in Supporting Information S1). Also shown are data from two other 3D seismic surveys (Io-Jansz and Thebe) from the Exmouth Plateau, although the exact relation of each pit crater to underlying structure is unknown (Velayatham et al., 2019).

Subsided strata within our studied pit craters typically have a lower amplitude and/or higher variance expression compared to reflections in the flanking host rock (Figures 4a, 6, and 7). These seismic attribute changes indicate less seismic energy was reflected back to the surface from within the pit crater, perhaps due to increased scattering of seismic energy from and/or local decreases in acoustic impedance across disrupted bedding (Brown, 2011). Both these controls on the amount of seismic energy reflected could be linked to disaggregation of and fluid infiltration through rock during or after subsidence, which are likely common processes that affect pit craters (e.g., Frumkin & Naor, 2019; Halliday, 1998; Velayatham et al., 2018).
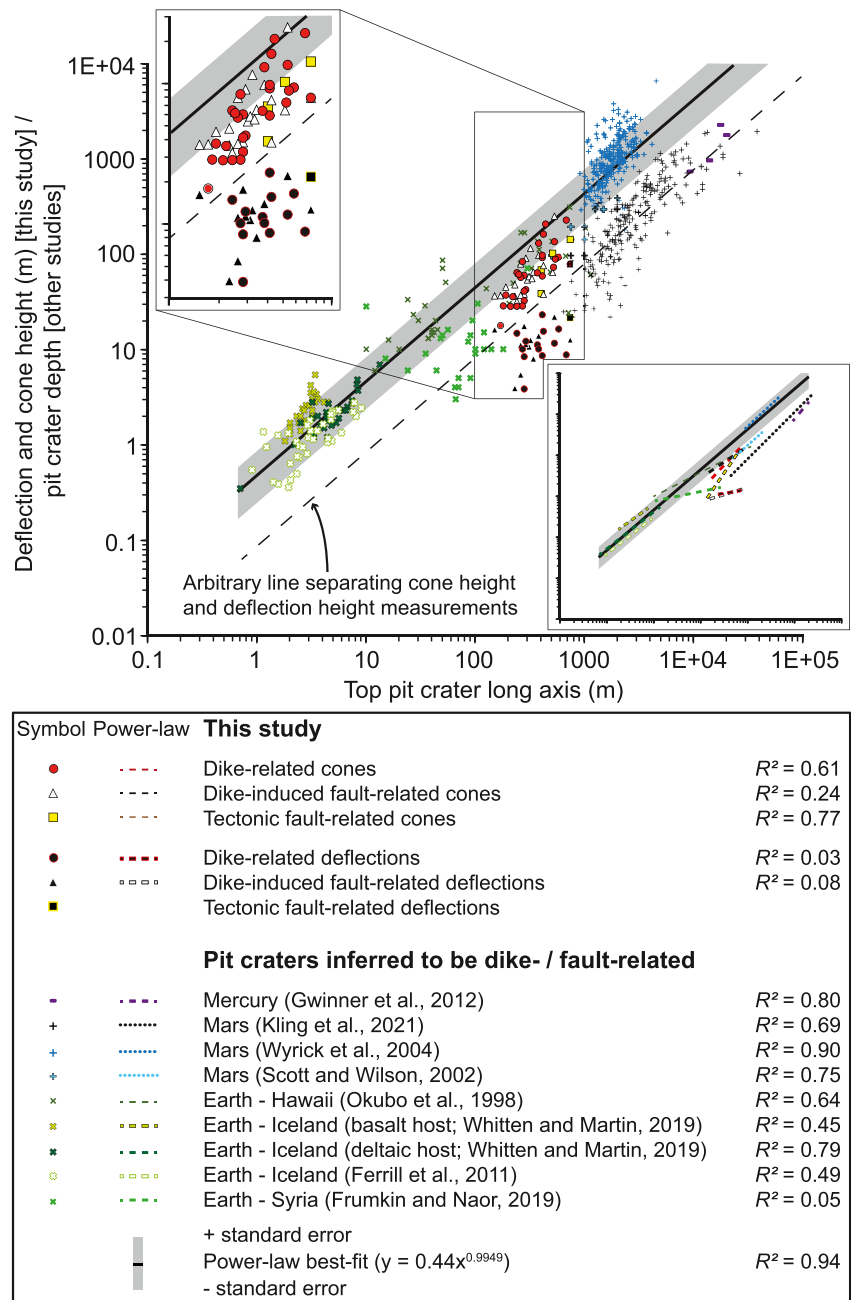
**Figure 11.** Log-log plot of cone height and deflection height, one of which is expected to be the equivalent to pit crater depth (e.g., Wyrick et al., 2004), compared with pit crater long axis lengths. Insets show a zoomed-in view of our data and the power-law best-fit trendlines for each plotted data set. The power-law best-fit trendline shown (black line) with standard errors was calculated from all literature data plotted, with the exception of data from Frumkin and Naor (2019) and Kling et al. (2021) as these pit craters show evidence of post-formation modification. We define an arbitrary boundary between areas where pit crater geometries are likely original (areas above the line) and those where infilling and/or erosion may have modified apparent pit crater depths (areas below the line).

### 5.1.2. Pit Crater Age

Defining the age of pit craters may help determine whether their formation was synchronous with tectonic or magmatic events, and thus potentially shed light on how they formed. Where data resolution allows, some reflections we observe above the pit craters appear thickened (e.g., F13; Figure 6d) and/or show onlap onto the conical walls of pits (e.g., G10a; Figure 6f). These seismic-stratigraphic relationships imply that the strata represented

by these reflections were deposited *within* the pit craters; that is, the pit craters were surficial features, similar to those recently formed on Earth (Abelson et al., 2003; Frumkin & Naor, 2019; Okubo & Martel, 1998; Whitten & Martin, 2019). We can thus use biostratigraphic data from local boreholes to estimate the age of reflections that marked the contemporaneous surface during pit crater formation.

The youngest pit craters (B1-3, D1-2) formed coincident with the Base Cretaceous unconformity at ∼148 Ma (Figure 9a; Figures S2b and S2d in Supporting Information S1). However, we note that the uppermost expression of most pit craters across the study area and along individual chains (e.g., A–C, E, F, H, and I) often occur below the Base Cretaceous unconformity at different stratigraphic horizons above the ∼165 Ma Top Athol Formation (Figures 6, 7, 9a, and 9b). For some pit crater chains, specifically D1-D2 and G1-G13, the tops of individual pits occur along the same stratigraphic horizon, suggesting these depressions formed near-synchronously (Figures 6e, 9a, and 9b). Our observations indicate the pit craters developed periodically during deposition of the marine Dingo Claystone in the Late Jurassic. Given the deep marine setting and continuous deposition of the Dingo Claystone (Tindale et al., 1998), we consider it likely that most pit craters were buried relatively quickly, and that any post-emplacement modification by erosion was minimal.

Our inferred Late Jurassic timing of pit crater formation is consistent with seismic-stratigraphic constraints on the age of the Exmouth Dike Swarm and associated dike-induced faults (Figure 2) (Magee & Jackson, 2020b). As most pit craters are found below the ∼148 Ma Base Cretaceous unconformity, but all dike-induced faults offset this horizon, it seems likely that pit crater formation generally ceased before dyking and associated faulting fully ended (Figures 4b and 4c) (Magee & Jackson, 2020b). We therefore suggest that, at least in part, the oldest pit craters occurred during the earliest development of the Exmouth Dike Swarm and associated dike-induced faults, with dyking and fault growth occurring (periodically) up until ∼148 Ma.

### 5.1.3. Pit Crater Origin

Numerous processes involving underlying cavity collapse or the volumetric reduction of a subsurface body have previously been proposed to generate space for overburden subsidence and pit crater formation (Figure 1) (see Wyrick et al., 2004 and references therein). We identify no clear cavity-like structures at the pit crater bases (e.g., Figures 3a, 4a, 6, and 7), and disregard the following possible mechanisms of pit crater formation: (a) carbonate or salt dissolution (Figure 1a) (Abelson et al., 2003; Spencer & Fanale, 1990), because the Triassic-to-Late Jurassic strata hosting the pit craters contains no (or only very little) carbonate rocks and no salt (Figure 2b) (e.g., Exon et al., 1992; Stagg et al., 2004; Tindale et al., 1998); (b) evacuation of lava tubes (see Sauro et al., 2020 and references therein), as there is no evidence for high-amplitude, sinuous, strata-concordant reflections that could be attributed to lava flows or tubes (e.g., Sun et al., 2019); and (c) magma migration from a reservoir (e.g., Mège et al., 2003; Poppe et al., 2015), as there is no evidence for underlying, tabular igneous intrusions (e.g., sills or laccoliths), which are typically expressed as high-amplitude, positive, sub-horizontal-to-inclined reflections (e.g., Planke et al., 2005).

We find that some pit craters directly are physically connected to either the upper tips of dikes ($n = 6$), dike-induced fault planes ($n = 6$), or tectonic faults ($n = 5$) (Figures 6 and 7). Where we observe pit crater bases situated some distance above dike upper tips or dike-induced faults (Figures 6 and 7), we consider it plausible that seismically unresolved or obscured portions of their pipes extend down to these underlying structures. The generation of pit craters linked to dike tips may be driven by (Figure 1f): (a) a volume reduction of the dike itself, perhaps as magma pressure wanes or volatiles escape (e.g., Patterson et al., 2016; Scott & Wilson, 2002); (b) the escape of heated pore fluids from the tip-adjacent host rock and subsequent porosity collapse (e.g., Schofield et al., 2010); (c) phreatic eruption (Hughes et al., 2018); and/or (iv) the subsidence of material into a tensile fracture that opens above an inflating and widening dike (similar to Figure 1d) (e.g., Ferrill et al., 2011; Smart et al., 2011; Tanaka & Golombek, 1989). The tops of individual pits located directly above dikes occur at deeper stratigraphic levels and are thus older toward the north of our study area (e.g., above dikes A and I; Figures 9a and 9b). These occurrences of pit crater tops at multiple stratigraphic levels above single dikes indicate that periods of sediment deposition separated pit crater formation (Figure 12); this interpretation is consistent with fault displacement data, which reveals that the dike-induced faults likely grew incrementally via segment linkage (Magee & Jackson, 2020a). As the dikes are part of a radial dike swarm that intruded laterally northwards (Figure 2a) (Magee & Jackson, 2020b), the apparent southwards decrease in age of the pit craters suggests that they did not develop above actively, northwards propagating dike tips (Figure 12a). Dike thickness also appears to decrease gradually northwards (Magee & Jackson, 2020b), so it seems unlikely that pit crater formation occurred in response to dike widening
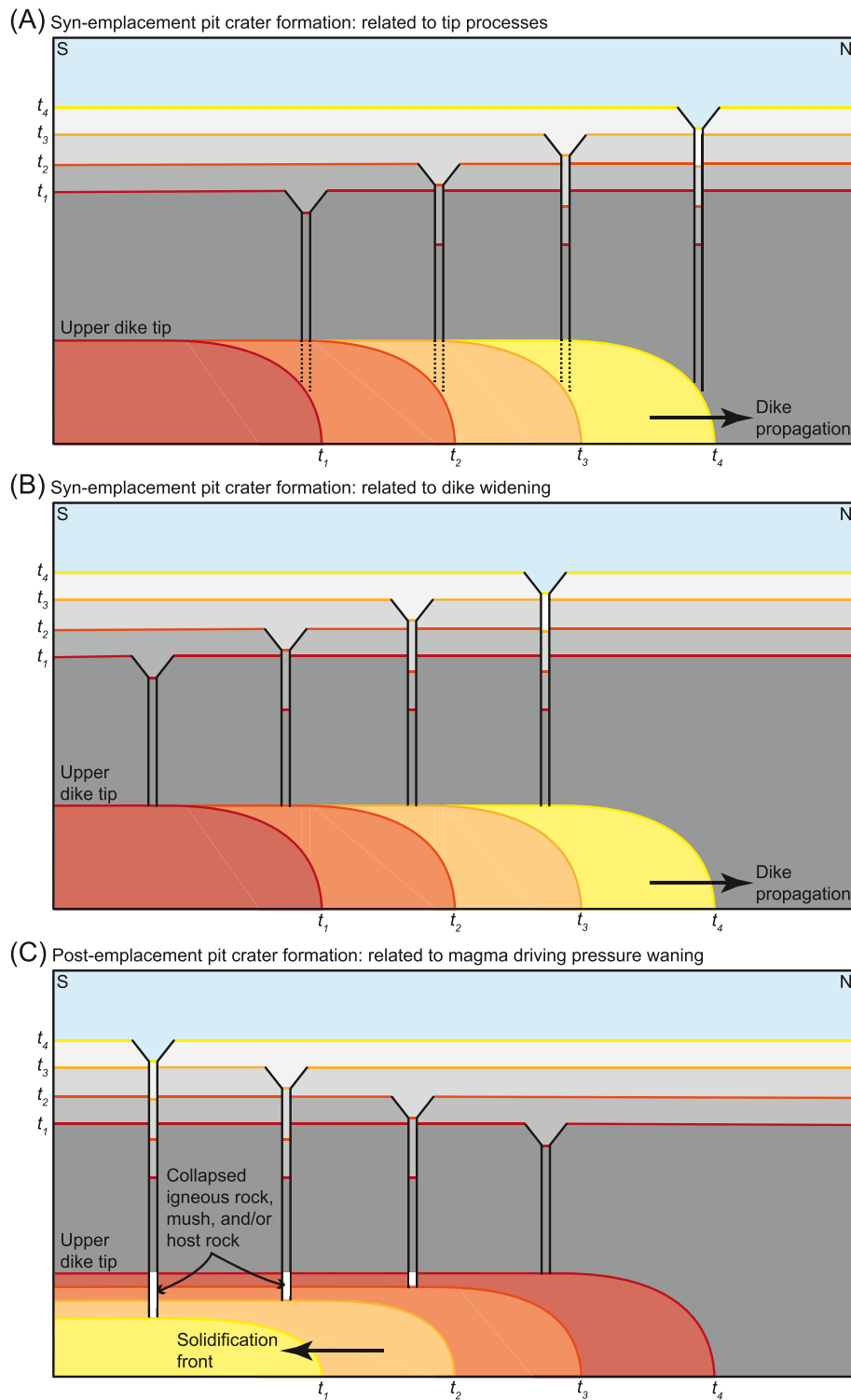
**Figure 12.** Schematic models showing how pit craters may be expected to relate to different dike processes. (a) Pit crater formation is linked to lateral propagation of the dike tip, perhaps driven by fluid escape into and/or collapse of the tip cavity, or eruption from the dike (Hughes et al., 2018; Scott & Wilson, 2002). Pit crater age decreases farther from the dike source. (b) Pit crater formation occurs as the dike widens behind the propagating tip, perhaps linked to tensile fracturing (Tanaka & Golombek, 1989) as dike widening induces extension of the overlying rock, fluid escape into and/or collapse of the tip cavity, or eruption (Hughes et al., 2018; Scott & Wilson, 2002). Again, pit crater age decreases farther from the dike source. (c) Pit crater formation occurs as the magma driving pressure or supply wanes, causing magma to flow backwards (e.g., Philpotts & Asher, 1994) and/or solidify and contract (i.e., a volume reduction) (e.g., Caricchi et al., 2014). In this scenario, pit crater age increases farther from the dike source.

and tensile fracturing of the overburden; under such a situation, we would expect the earliest pit craters to form where dike width is greatest (Figure 12b). We suggest that the possible southwards decrease in age of pit craters directly above dikes may have resulted because of localized volume reductions of the intrusion as driving pressure periodically waned (Figure 12c). Such volume reductions could have been controlled by magma backflow and retreat (e.g., Philpotts & Asher, 1994; Philpotts & Philpotts, 2007), or solidification and contraction (e.g., Caricchi et al., 2014). Cyclical periods of intrusion and driving pressure waning could create complex trends of pit craters along individual dikes.

Pit craters linked to faults elsewhere on the Exmouth Plateau have been referred to as "pockmarks" and attributed to a local reduction of confining pressure and fluid escape from an overpressured horizon in the Mungaroo Formation during faulting (e.g., Figure 1b) (Velayatham et al., 2018, 2019); our data are consistent with this interpretation. We thus consider it plausible that some pit craters formed in response to fluid escape from within the Mungaroo Formation, instigated by dike-induced faulting or dike-synchronous reactivation of Early Jurassic tectonic faults (e.g., Figure 1b) (Velayatham et al., 2018, 2019). We also show that some pit craters link to steep-to-sub-vertical fault portions, suggesting that their formation may also be associated with the collapse of dilatational jogs (Figure 1e, 7b, 8b, and 8c) (e.g., Ferrill et al., 2011; Ferrill & Morris, 2003; Ketterman et al., 2015; Kettermann et al., 2019; Smart et al., 2011; Von Hagke et al., 2019). Our observations also allow for the generation of these pit craters in response to the opening of vertical tensile fractures (Figure 1d) (e.g., Ferrill et al., 2011; Smart et al., 2011; Tanaka & Golombek, 1989), which cannot be directly imaged in these seismic reflection data.

## 5.2. Comparison With Pit Craters Elsewhere on Earth and Other Planetary Bodies

The surface expression of pit craters observed on Earth and other planetary bodies has been used to infer how they formed, and to establish dynamic characteristics of otherwise inaccessible subsurface geology (e.g., Hardy, 2021; Kling et al., 2021; Korteniemi et al., 2010; Martin et al., 2017; Mège & Masson, 1997; Smart et al., 2011; Whitten & Martin, 2019). By showing how pit craters link to dikes and faults at depth (Figures 3a, 4a, 6, and 7), at least for some pit craters on Earth, we provide the first validation that dyking and faulting processes could drive extraterrestrial pit crater formation (e.g., Ferrill et al., 2011; Ferrill & Morris, 2003; Ketterman et al., 2015; Kettermann et al., 2019; Mège & Masson, 1996; Okubo & Martel, 1998; Scott & Wilson, 2002; Smart et al., 2011; Von Hagke et al., 2019). However, we also demonstrate that there are no significant differences in the size or orientation of pit craters regardless of whether they developed above dikes, dike-induced faults, or tectonic faults (Figures 8, 10 and 11). Although our data thus suggest it is viable to invoke dyking and faulting processes as drivers of pit crater formation, they also imply that the surficial size and orientation of pit craters may not be diagnostic of any specific formation mechanism(s).

Even if the surface expression of pit craters does not reflect their generational mechanism(s), it is plausible that pit size and shape are controlled by the subsurface geology and/or prevailing stress conditions (e.g., Whitten & Martin, 2019). To apply the implications of our findings for understanding the controls on extraterrestrial pit crater surface expression elsewhere, we first need to establish whether the pit craters we analyze are appropriate analogs to those on other worlds. In particular, our pit craters formed during deposition of the Dingo Claystone in a marine environment (Tindale et al., 1998). An overburden pressure controlled by water depth was thus exerted on our pit craters during their development, but pits formed elsewhere are typically considered to have formed at a free surface (e.g., see Wyrick et al., 2004 and references therein). Furthermore, the shallow sub-seabed material contemporaneous to pit crater formation was likely unconsolidated, very fine-grained, *and* wet. Typically, we might expect the presence of abundant pore fluids to alter the syn-deformation behavior of sediment (or soil) compared to dry, unconsolidated materials (e.g., dry regolith) on Earth and other planetary bodies (e.g., Johansson & Konagai, 2006). For example, dry regolith may catastrophically collapse into an open cavities (e.g., Hardy, 2021), whereas wet clays that are cohesive and may instead sag into voids (e.g., Beck, 1988). Despite these potential differences in rheology, it seems reasonable to expect unconsolidated materials to respond similarly to localized subsidence, regardless of whether they are wet, dry, or have variable cohesion; that is, they should drain/collapse/sag into underlying voids (e.g., Beck, 1988; Hardy, 2021). By assuming to a first order that the drainage of wet or dry material into a pipe eventually results in localized subsidence that produces a depression at the surface (e.g., Beck, 1988), then we consider our pit craters as comparable to those developed elsewhere. Physical and numerical modeling is required to fully test this hypothesis.

### 5.2.1. Pit Crater Depth

Where pit craters are observed on the surface of Earth and other planetary bodies, we are typically restricted to measuring their plan-view geometry (e.g., axial dimensions) and crater depth (e.g., Whitten & Martin, 2019; Wyrick et al., 2004). Previous studies that have linked pit craters to dike or fault activity suggest pit crater depths positively correlate with their long axis lengths via power-law relationships ($R^2$ = 0.45–0.90) with similar slopes (Figure 11) (e.g., Ferrill et al., 2011; Gwinner et al., 2012; Kling et al., 2021; Okubo & Martel, 1998; Scott & Wilson, 2002; Whitten & Martin, 2019; Wyrick et al., 2004); these data can be fit by a single power-law relationship ($R^2$ = 0.94; Figure 11). Yet some potentially dike- or fault-related pit craters show no correlation between pit crater depth and long axis length, such as those in the Golan volcanic province, southern Levant ($R^2$ = 0.05; Figure 11). Similarly, those pit craters widespread in Noctis Labyrinthus (Mars) have dimensions up to an order of magnitude below the power-law trend described by published data (Figure 11) (Frumkin & Naor, 2019; Kling et al., 2021). These deviations from the main power-law trend have been attributed to post-emplacement modification by erosion and sedimentation, causing pit craters to become shallower and wider with time (Frumkin & Naor, 2019; Kling et al., 2021).

From our seismic reflection data, we can measure pit crater morphometric properties, but need to establish whether the height of the inverted cone sections, or that of the deflected reflections they contain, are equivalent to pit crater depth (Figure 3b). For pit craters above dikes, dike-induced faults, and tectonic faults, we find that cone height and pit long axis length positively correlate at least to some extent ($R^2$ = 0.61, 0.24, and 0.77, respectively) and overlap with data from many other locations (Figure 11). However, there is no meaningful correlation ($R^2$ = <0.1) for deflection height and pit long axis length (Figure 11). The deflection height measurements also fall an order of magnitude below the power-law trend fit to the compiled published pit crater data; this trend is similar to pit craters in Noctis Labyrinthus (Mars), which display evidence for post-formation modification of their initial geometries (Figure 11) (Kling et al., 2021). Based on these comparisons, we suggest that the walls of the inverted cone sections represent the original pit crater morphology; that is, cone height is equivalent to pit crater depth. The correlation between our measured pit crater depths and lengths, and their overlap with data trends from pits elsewhere, justifies the view that our pit craters are analogous to those elsewhere and implies that any reduction of cone height for our pits by burial-related compaction was minimal (Figure 11). The reflections within the inverted cone sections are interpreted to correspond to material that infilled the pit crater. Our results support recent suggestions that relationships between pit crater depths and long axis lengths *can* provide some indication as to whether post-formation erosional and infilling processes have widened and reduced the depth of pit geometry (Figure 11) (Frumkin & Naor, 2019; Kling et al., 2021).

### 5.2.2. Pit Crater Depth and Regolith Thickness

Pit crater depths have been used as a proxy for minimum regolith thickness on other planetary bodies (e.g., Whitten & Martin, 2019; Wyrick et al., 2004). This use of pit crater depth follows the inference that drainage of loose, unconsolidated material into an underlying cavity instigates development of an inverted cone section controlled by the host materials angle of repose (e.g., Whitten & Martin, 2019; Wyrick et al., 2004); that is, the transition from the pit to underlying pipe occurs at the boundary between rock and regolith, if the cavity is of sufficient volume relative to the regolith thickness (Hardy, 2021). We show that cone height (i.e., pit crater depth) varies non-systematically across the study area, including along individual chains, with adjacent pit craters of the same age often displaying different cone heights (Figures 6, 7, and 9c). Furthermore, some pit craters seemingly have no seismically resolved inverted cone section and appear simply to have a pipe-like geometry (Figures 6 and 7). Under the assumption that the transition from unconsolidated wet sediment to lithified rock (i.e., perhaps equivalent to a regolith-rock transition) occurred at a relatively constant depth across the study area, the observed variation in pit crater cone heights and occasional absence of inverted cone sections suggest the changing rheology of the host material did not primarily control pit crater geometry (cf. Whitten & Martin, 2019; Wyrick et al., 2004). Our results support suggestions that other influences (e.g., pit spacing, pipe volume, lateral variations in sediment type), in conjunction with a rheological change between lithified rock and unconsolidated sediment/regolith, were the main controls on pit crater depth (e.g., Whitten & Martin, 2019; Wyrick et al., 2004).

### 5.2.3. Pit Crater Elongation

We might expect pit craters' long axes, like that of volcanic vents, to be aligned parallel to underlying dikes or faults as they form within the same stress field (Bonini & Mazzarini, 2010; Magee et al., 2016; Paulsen &

Wilson, 2010). Yet the pit craters we analyze show no preferred long axis orientations, even those seemingly related to contemporaneous dikes and dike-induced faults, both of which are clearly aligned ~N-S in our study area (Figure 5). This disparity in dike/fault orientation relative to pit crater long axes implies pit crater formation was not sensitive to the prevailing stress field; we hypothesize that the drainage mechanics of unconsolidated sediment, and proximity to adjacent pit craters, likely dominates the elongation of pit craters as a local phenomenon, as opposed to the prevailing but regional stress field.

## 6. Conclusions

We use seismic reflection data from offshore NW Australia to image the full 3D geometry of pit craters and underlying magmatic and tectonic structures. Our work demonstrates that pit craters in our data link at depth to dikes and steep fault segments, confirming the hypothesis that pit crater formation can occur in response to magmatic processes and dilatational faulting. We also show that pit crater depths strongly correlate with their long axis lengths, consistent with observations of pit craters elsewhere on Earth and other planetary bodies; deviation of pit crater populations from the power-law trend that defines these may be an indicator that pit craters have been infilled and/or modified following their formation. Our results suggest that we should be cautious when interpreting the origin of pit craters on other planetary bodies because: (a) the distribution and size of pit craters may not be diagnostic of the potential dyking and/or faulting processes driving their formation; and (b) there are many factors that can control pit crater size, including the mechanical properties of the host material (e.g., regolith). Overall, our work shows that reflection seismology is a powerful tool for understanding the subsurface structure and properties of this and other worlds, allowing us to examine the 3D structure of features on Earth thought analogous to those recognised on the surfaces of other planetary bodies.

## Data Availability Statement

Seismic reflection and well data used in this study are freely available from either the Geoscience Australia NOPIMS (https://nopims.dmp.wa.gov.au/nopims) data repository or that of the UK National Geoscience Data Centre (NGDC; https://www.bgs.ac.uk/geological-data/national-geoscience-data-centre/). The NOPIMS data access centre allows "Wells" (i.e., for this study Chandon 1, Chandon 2, Chandon 3, Mercury 1, and Yellowglen 1) and "Surveys" (i.e., for this study the Chandon 3D MSS seismic reflection survey) from offshore Australia to be searched for. From these search results, well data can be downloaded by highlighting the correct well and using "view details for selected rows"; due to the file size of seismic reflection segy data like the Chandon 3D MSS, few can be downloaded but all can be added to a basket and requested from Geoscience Australia. These data can also be downloaded from the NGDC under the title "3D seismic reflection surveys (Chandon and Glencoe) and borehole data from offshore NW Australia." All measurements and calculations acquired during this research are provided in Table S1 in Supporting Information S1 and a copy is also hosted in the NGDC (Magee, 2022).

## References

Abelson, M., Baer, G., Shtivelman, V., Wachs, D., Raz, E., Crouvi, O., et al. (2003). Collapse-sinkholes and radar interferometry reveal neotectonics concealed within the Dead Sea basin. *Geophysical Research Letters*, *30*(10), 1545. https://doi.org/10.1029/2003gl017103

Beck, B. F. (1988). Environmental and engineering effects of sinkholes—The processes behind the problems. *Environmental Geology and Water Sciences*, *12*(2), 71–78. https://doi.org/10.1007/bf02574791

Bilal, A., McClay, K., & Scarselli, N. (2018). *Fault-scarp degradation in the central Exmouth Plateau, north west shelf, Australia* (Vol. 476, pp. SP476–411). Geological Society, London, Special Publications.

Black, M., McCormack, K., Elders, C., & Robertson, D. (2017). Extensional fault evolution within the Exmouth Sub-basin, north west shelf, Australia. *Marine and Petroleum Geology*, *85*, 301–315. https://doi.org/10.1016/j.marpetgeo.2017.05.022

Bonini, M., & Mazzarini, F. (2010). Mud volcanoes as potential indicators of regional stress and pressurized layer depth. *Tectonophysics*, *494*(1), 32–47. https://doi.org/10.1016/j.tecto.2010.08.006

Brown, A. R. (2011). *Interpretation of three-dimensional seismic data*. 6th ed., (Vol. 42). AAPG and SEG.

Caricchi, L., Biggs, J., Annen, C., & Ebmeier, S. (2014). The influence of cooling, crystallisation and re-melting on the interpretation of geodetic signals in volcanic systems. *Earth and Planetary Science Letters*, *388*, 166–174. https://doi.org/10.1016/j.epsl.2013.12.002

Chopra, S., & Marfurt, K. J. (2005). Seismic attributes—A historical perspective. *Geophysics*, *70*(5), 3SO–28SO. https://doi.org/10.1190/1.2098670

Direen, N. G., Stagg, H. M. J., Symonds, P. A., & Colwell, J. B. (2008). Architecture of volcanic rifted margins: New insights from the Exmouth – Gascoyne margin, Western Australia. *Australian Journal of Earth Sciences*, *55*(3), 341–363. https://doi.org/10.1080/08120090701769472

Driscoll, N. W., & Karner, G. D. (1998). Lower crustal extension across the Northern Carnarvon basin, Australia: Evidence for an eastward dipping detachment. *Journal of Geophysical Research*, *103*(B3), 4975–4991. (1978–2012). https://doi.org/10.1029/97jb03295

Exon, N., Haq, B., & Von Rad, U. (1992). Exmouth Plateau revisited: Scientific drilling and geological framework. In *Paper presented at the proceedings of the ocean drilling program, scientific results*.

Ferrill, D. A., & Morris, A. P. (2003). Dilational normal faults. *Journal of Structural Geology*, *25*(2), 183–196. https://doi.org/10.1016/s0191-8141(02)00029-9

Ferrill, D. A., Wyrick, D. Y., Morris, A. P., Sims, D. W., & Franklin, N. M. (2004). Dilational fault slip and pit chain formation on Mars. *Geological Society of America Today*, *14*(10), 4. https://doi.org/10.1130/1052-5173(2004)014<4:dfsapc>2.0.co;2

Ferrill, D. A., Wyrick, D. Y., & Smart, K. J. (2011). Coseismic, dilational-fault and extension-fracture related pit chain formation in Iceland: Analog for pit chains on Mars. *Lithosphere*, *3*(2), 133–142. https://doi.org/10.1130/l123.1

Frumkin, A., & Naor, R. (2019). Formation and modification of pit craters–example from the Golan volcanic plateau, southern Levant. *Zeitschrift für Geomorphologie*, *62*(3), 163–181. https://doi.org/10.1127/zfg/2019/0614

Gartrell, A., Torres, J., Dixon, M., & Keep, M. (2016). Mesozoic rift onset and its impact on the sequence stratigraphic architecture of the Northern Carnarvon Basin. *The APPEA Journal*, *56*(1), 143–158. https://doi.org/10.1071/aj15012

Gwinner, K., Head, J. W., Oberst, J., Gillis-Davis, J. J., Xiao, Z., Strom, R. G., et al. (2012). Morphology of pit craters on Mercury from stereo-derived topography and implications for pit crater formation. In *Lunar and Planetary Science Conference* (No. 1659, p. 1991).

Halliday, W. R. (1998). "Pit craters", lava tubes, and open vertical volcanic conduits in Hawaii: A problem in terminology. *International Journal of Speleology*, *27*(1), 113–124. https://doi.org/10.5038/1827-806x.27.1.12

Hardy, S. (2021). Discrete element modelling of pit crater formation on Mars. *Geosciences*, *11*(7), 268. https://doi.org/10.3390/geosciences11070268

Hocking, R. (1992). *Jurassic deposition in the southern and central north west shelf*. Geological Survey Western Australia Record.199217.

Hocking, R. M., Moors, H. T., & Van de Graaff, W. E. (1987). *Geology of the carnarvon basin* (Vol. 133). State Print Division.

Horstman, K., & Melosh, H. (1989). Drainage pits in cohesionless materials: Implications for the surface of Phobos. *Journal of Geophysical Research*, *94*(B9), 12433–12441. https://doi.org/10.1029/jb094ib09p12433

Hughes, S. S., Nawotniak, S. E. K., Sears, D. W., Borg, C., Garry, W. B., Christiansen, E. H., et al. (2018). Phreatic explosions during basaltic fissure eruptions: Kings Bowl lava field, Snake River Plain, USA. *Journal of Volcanology and Geothermal Research*, *351*, 89–104. https://doi.org/10.1016/j.jvolgeores.2018.01.001

Johansson, J., & Konagai, K. (2006). Fault induced permanent ground deformations—An experimental comparison of wet and dry soil and implications for buried structures. *Soil Dynamics and Earthquake Engineering*, *26*(1), 45–53. https://doi.org/10.1016/j.soildyn.2005.08.003

Ketterman, M., Grützner, C., Urai, J., Reicherter, K., & Mertens, J. (2015). Evolution of a highly dilatant fault zone in the grabens of Canyonlands National Park, Utah, USA–integrating fieldwork, ground-penetrating radar and airborne imagery analysis. *Solid Earth*, *6*(3), 839–855. https://doi.org/10.5194/se-6-839-2015

Kettermann, M., Weismüller, C., von Hagke, C., Reicherter, K., & Urai, J. L. (2019). Large near-surface block rotations at normal faults of the Iceland rift: Evolution of tectonic caves and dilatancy. *Geology*, *47*(8), 781–785. https://doi.org/10.1130/g46158.1

Kling, C. L., Byrne, P. K., Atkins, R. M., & Wegmann, K. W. (2021). Tectonic deformation and volatile loss in the formation of Noctis Labyrinthus, Mars. *Journal of Geophysical Research: Planets*, *126*(11), e2020JE006555. https://doi.org/10.1029/2020je006555

Korteniemi, J., Raitala, J., Aittola, M., Ivanov, M. A., Kostama, V.-P., Öhman, T., & Hiesinger, H. (2010). Dike indicators in the hadriaca patera–promethei terra region, Mars. *Earth and Planetary Science Letters*, *294*(3), 466–478. https://doi.org/10.1016/j.epsl.2009.06.038

Longley, I., Buessenschuett, C., Clydsdale, L., Cubitt, C., Davis, R., Johnson, M., et al. (2002). The north west shelf of Australia–a woodside perspective. *The sedimentary basins of Western Australia*, *3*, 27–88.

Mège, D., Cook, A. C., Garel, E., Lagabrielle, Y., & Cormier, M. H. (2003). Volcanic rifting at Martian grabens. *Journal of Geophysical Research*, *108*(E5), 5044. https://doi.org/10.1029/2002je001852

Mège, D., & Masson, P. (1996). A plume tectonics model for the Tharsis province, Mars. *Planetary and Space Science*, *44*(12), 1499–1546. https://doi.org/10.1016/s0032-0633(96)00113-4

Mège, D., & Masson, P. (1997). Graben formation and dike emplacement on Earth and other planets. In *Paper presented at the lunar and planetary science conference*. (Vol. *28*, p.929).

Magee, C. (2022). Dyke-induced fault and pit crater measurements and predicted dyke properties offshore NW Australia [Dataset]. NERC EDS National Geoscience Data Centre. https://doi.org/10.5285/2EDF6C47-FD18-4540-B449-B78D12422193

Magee, C., Duffy, O. B., Purnell, K., Bell, R. E., Jackson, C. A. L., & Reeve, M. T. (2016). Fault-controlled fluid flow inferred from hydrothermal vents imaged in 3D seismic reflection data, offshore NW Australia. *Basin Research*, *28*(3), 299–318. https://doi.org/10.1111/bre.12111

Magee, C., Ernst, R. E., Muirhead, J., Phillips, T., & Jackson, C. A.-L. (2019). Magma transport pathways in large igneous provinces: Lessons from combining field observations and seismic reflection data. In R. Srivastava, R. Ernst, & P. Peng (Eds.), *Dyke swarms of the world: A modern perspective* (pp. 45–85). Springer.

Magee, C., & Jackson, C. A.-L. (2020a). Can we relate the surface expression of dike-induced normal faults to subsurface dike geometry? *Geology*, *49*(4), 366–371. https://doi.org/10.1130/g48171.1

Magee, C., & Jackson, C.A.-L. (2020b). Seismic reflection data reveal the 3D structure of the newly discovered Exmouth Dyke Swarm, offshore NW Australia. *Solid Earth*, *11*(2), 576–606. https://doi.org/10.5194/se-11-579-2020

Marfurt, K. J., & Alves, T. M. (2015). Pitfalls and limitations in seismic attribute interpretation of tectonic features. *Interpretation*, *3*(1), SB5–SB15. https://doi.org/10.1190/int-2014-0122.1

Marshall, N., & Lang, S. (2013). A new sequence stratigraphic framework for the North West Shelf, Australia. In *Paper presented at the the sedimentary basins of western Australia 4: Proceedings PESA symposium*.

Martin, E. S., Kattenhorn, S. A., Collins, G. C., Michaud, R. L., Pappalardo, R. T., & Wyrick, D. Y. (2017). Pit chains on Enceladus signal the recent tectonic dissection of the ancient cratered terrains. *Icarus*, *294*, 209–217. https://doi.org/10.1016/j.icarus.2017.03.014

Okubo, C. H., & Martel, S. J. (1998). Pit crater formation on Kilauea volcano, Hawaii. *Journal of Volcanology and Geothermal Research*, *86*(1), 1–18. https://doi.org/10.1016/s0377-0273(98)00070-5

Paganoni, M., King, J. J., Foschi, M., Mellor-Jones, K., & Cartwright, J. A. (2019). A natural gas hydrate system on the Exmouth Plateau (NW shelf of Australia) sourced by thermogenic hydrocarbon leakage. *Marine and Petroleum Geology*, *99*, 370–392. https://doi.org/10.1016/j.marpetgeo.2018.10.029

Partington, M., Aurisch, K., Clark, W., Newlands, I., Phelps, S., Senycia, P., et al. (2003). The hydrocarbon potential of exploration permits WA-299-P and WA-300-P, Carnarvon Basin: A case study. *The APPEA Journal*, *43*(1), 339–361. https://doi.org/10.1071/aj02018

Patterson, C. W., Ernst, R. E., & Samson, C. (2016). Pit chains belonging to radiating graben-fissure systems on Venus: Model for Formation during lateral dyke injection. *Acta Geologica Sinica*, *90*(s1), 143–144. https://doi.org/10.1111/1755-6724.12937

Paulsen, T. S., & Wilson, T. J. (2010). New criteria for systematic mapping and reliability assessment of monogenetic volcanic vent alignments and elongate volcanic vents for crustal stress analyses. *Tectonophysics*, *482*(1), 16–28. https://doi.org/10.1016/j.tecto.2009.08.025

Paumard, V., Bourget, J., Payenberg, T., Ainsworth, R. B., George, A. D., Lang, S., et al. (2018). Controls on shelf-margin architecture and sediment partitioning during a syn-rift to post-rift transition: Insights from the Barrow Group (northern Carnarvon Basin, north west shelf, Australia). *Earth-Science Reviews*, *177*, 643–677. https://doi.org/10.1016/j.earscirev.2017.11.026

Philpotts, A., & Asher, P. (1994). Magmatic flow-direction indicators in a giant diabase feeder dike, Connecticut. *Geology*, *22*(4), 363–366. https://doi.org/10.1130/0091-7613(1994)022<0363:mfdiia>2.3.co;2

Philpotts, A. R., & Philpotts, D. E. (2007). Upward and downward flow in a camptonite dike as recorded by deformed vesicles and the anisotropy of magnetic susceptibility (AMS). *Journal of Volcanology and Geothermal Research*, *161*(1–2), 81–94. https://doi.org/10.1016/j.jvolgeores.2006.11.006

Planke, S., Rasmussen, T., Rey, S. S., & Myklebust, R. (2005). Seismic characteristics and distribution of volcanic intrusions and hydrothermal vent complexes in the Vøring and Møre basins. In A. G. Doré (Ed.), *Petroleum geology: North-west europe and global perspectives - proceddings of the 6th petroleum geology conference* (pp. 833–844). Geological Society.

Poppe, S., Holohan, E. P., Pauwels, E., Cnudde, V., & Kervyn, M. (2015). Sinkholes, pit craters, and small calderas: Analog models of depletion-induced collapse analyzed by computed X-ray microtomography. *The Geological Society of America Bulletin*, *127*(1–2), 281–296. https://doi.org/10.1130/b30989.1

Reeve, M. T., Jackson, C. A. L., Bell, R. E., Magee, C., & Bastow, I. D. (2016). The stratigraphic record of prebreakup geodynamics: Evidence from the Barrow Delta, offshore Northwest Australia. *Tectonics*, *35*(8), 1935–1968. https://doi.org/10.1002/2016tc004172

Reeve, M. T., Magee, C., Bastow, I. D., McDermott, C., Jackson, C. A.-L., Bell, R. E., & Prytulak, J. (2021). Nature of the cuvier abyssal plain crust, offshore NW Australia. *Journal of the Geological Society*, *178*(5), jgs2020–172. https://doi.org/10.1144/jgs2020-172

Robb, M. S., Taylor, B., & Goodliffe, A. M. (2005). Re-Examination of the magnetic lineations of the gascoyne and cuvier abyssal plains, off NW Australia. *Geophysical Journal International*, *163*(1), 42–55. https://doi.org/10.1111/j.1365-246x.2005.02727.x

Sauro, F., Pozzobon, R., Massironi, M., De Berardinis, P., Santagata, T., & De Waele, J. (2020). Lava tubes on Earth, Moon and Mars: A review on their size and morphology revealed by comparative planetology. *Earth-Science Reviews*, *209*(103288). https://doi.org/10.1016/j.earscirev.2020.103288

Schofield, N., Stevenson, C., & Reston, T. (2010). Magma fingers and host rock fluidization in the emplacement of sills. *Geology*, *38*(1), 63–66. https://doi.org/10.1130/g30142.1

Sclater, J. G., & Christie, P. A. (1980). Continental stretching: An explanation of the post-mid-Cretaceous subsidence of the central North Sea basin. *Journal of Geophysical Research*, *85*(B7), 3711–3739. https://doi.org/10.1029/jb085ib07p03711

Scott, E. D., & Wilson, L. (2002). Plinian eruptions and passive collapse events as mechanisms of formation for Martian pit chain craters. *Journal of Geophysical Research*, *107*(E4), 4-1–4-11. https://doi.org/10.1029/2000je001432

Smart, K. J., Wyrick, D. Y., & Ferrill, D. A. (2011). Discrete element modeling of Martian pit crater formation in response to extensional fracturing and dilational normal faulting. *Journal of Geophysical Research*, *116*(E4), E04005. https://doi.org/10.1029/2010je003742

Spencer, J. R., & Fanale, F. P. (1990). New models for the origin of Valles Marineris closed depressions. *Journal of Geophysical Research*, *95*(B9), 14301–14313. https://doi.org/10.1029/jb095ib09p14301

Stagg, H., Alcock, M., Bernardel, G., Moore, A., Symonds, P., & Exon, N. (2004). Geological framework of the outer Exmouth Plateau and adjacent ocean basins. *Geoscience*.

Stagg, H., & Colwell, J. (1994). The structural foundations of the northern Carnarvon Basin. In *Paper presented at the the sedimentary basins of western Australia: Proceedings of petroleum exploration society of Australia symposium*.

Sun, Q., Jackson, C. A.-L., Magee, C., Mitchell, S. J., & Xie, X. (2019). Extrusion dynamics of deepwater volcanoes revealed by 3-D seismic data. *Solid Earth*, *10*(4), 1269–1282. https://doi.org/10.5194/se-10-1269-2019

Tanaka, K., & Golombek, M. (1989). Martian tension fractures and the formation of grabens and collapse features at Valles Marineris. In *Paper presented at the lunar and planetary science conference proceedings*.

Tindale, K., Newell, N., Keall, J., & Smith, N. (1998). Structural evolution and charge history of the Exmouth Sub-basin, northern Carnarvon Basin, Western Australia. In *Paper presented at the the sedimentary basins of western Australia 2: Proceedings of petroleum society Australia symposium*.

Velayatham, T., Holford, S., Bunch, M., King, R., & Magee, C. (2019). 3D seismic analysis of ancient subsurface fluid flow in the Exmouth Plateau, offshore Western Australia. In *Paper presented at the west Australian basins symposium*.

Velayatham, T., Holford, S. P., & Bunch, M. A. (2018). Ancient fluid flow recorded by remarkably long, buried pockmark trains observed in 3D seismic data, Exmouth Plateau, Northern Carnarvon basin. *Marine and Petroleum Geology*, *95*, 303–313. https://doi.org/10.1016/j.marpetgeo.2018.05.007

Von Hagke, C., Kettermann, M., Bitsch, N., Bücken, D., Weismüller, C., & Urai, J. L. (2019). The effect of obliquity of slip in normal faults on distribution of open fractures. *Frontiers of Earth Science*, *7*(18). https://doi.org/10.3389/feart.2019.00018

Wall, M., Cartwright, J., Davies, R., & McGrandle, A. (2010). 3D seismic imaging of a tertiary dyke swarm in the southern north sea, UK. *Basin Research*, *22*(2), 181–194. https://doi.org/10.1111/j.1365-2117.2009.00416.x

Whitten, J. L., & Martin, E. S. (2019). Icelandic pit chains as planetary analogs: Using morphologic measurements of pit chains to determine regolith thickness. *Journal of Geophysical Research: Planets*, *124*(11), 2983–2999. https://doi.org/10.1029/2019je006099

Wyrick, D. (2004). Distribution, morphology, and origins of Martian pit crater chains. *Journal of Geophysical Research*, *109*(E6), E06005. https://doi.org/10.1029/2004je002240

Wyrick, D., Ferrill, D. A., Morris, A. P., Colton, S. L., & Sims, D. W. (2004). Distribution, morphology, and origins of Martian pit crater chains. *Journal of Geophysical Research*, *109*(E6), E06005. https://doi.org/10.1029/2004je002240

Wyrick, D. Y., Morris, A. P., Todt, M. K., & Watson-Morris, M. J. (2015). Physical analogue modelling of Martian dyke-induced deformation. *Geological Society, London, Special Publications*, *401*(1), 395–403. https://doi.org/10.1144/sp401.15

Yang, X.-M., & Elders, C. (2016). The mesozoic structural evolution of the gorgon platform, North Carnarvon basin, Australia. *Australian Journal of Earth Sciences*, *63*(6), 755–770. https://doi.org/10.1080/08120099.2016.1243579